J. Plasma Phys. (2019), *vol.* 85, 905850506 © Cambridge University Press 2019
doi:10.1017/S0022377819000631

ViDA: a Vlasov–DArwin solver for plasma physics at electron scales

Oreste Pezzi[1,2,3,†], **Giulia Cozzani**[4,5], **Francesco Califano**[4], **Francesco Valentini**[3], **Massimiliano Guarrasi**[6], **Enrico Camporeale**[7,8], **Gianfranco Brunetti**[3], **Alessandro Retinò**[5] **and Pierluigi Veltri**[3]

[1]Gran Sasso Science Institute, Viale F. Crispi 7, I-67100 LAquila, Italy

[2]INFN/Laboratori Nazionali del Gran Sasso, Via G. Acitelli 22, I-67100 Assergi (AQ), Italy

[3]Dipartimento di Fisica, Università della Calabria, Via P. Bucci, I-87036 Arcavacata di Rende (CS), Italy

[4]Dipartimento di Fisica 'E. Fermi', Università di Pisa, Largo B. Pontecorvo 3, I-56127 Pisa, Italy

[5]Laboratoire de Physique des Plasmas, CNRS/École Polytechnique/Sorbonne Université, Université Paris Sud, Observatoire de Paris, 91128 Palaiseau, France

[6]CINECA Interuniversity Consortium, Via Magnanelli 6/3, 40033 Casalecchio di Reno, Italy

[7]CIRES, University of Colorado, Boulder, CO, USA

[8]Center for Mathematics and Computer Science (CWI), 1090 GB Amsterdam, The Netherlands

(Received 3 May 2019; revised 7 September 2019; accepted 9 September 2019)

We present a Vlasov–DArwin numerical code (ViDA) specifically designed to address plasma physics problems, where small-scale high accuracy is requested even during the nonlinear regime to guarantee a clean description of the plasma dynamics at fine spatial scales. The algorithm provides a low-noise description of proton and electron kinetic dynamics, by splitting in time the multi-advection Vlasov equation in phase space. Maxwell equations for the electric and magnetic fields are reorganized according to the Darwin approximation to remove light waves. Several numerical tests show that ViDA successfully reproduces the propagation of linear and nonlinear waves and captures the physics of magnetic reconnection. We also discuss preliminary tests of the parallelization algorithm efficiency, performed at CINECA on the Marconi-KNL cluster. ViDA will allow the running of Eulerian simulations of a non-relativistic fully kinetic collisionless plasma and it is expected to provide relevant insights into important problems of plasma astrophysics such as, for instance, the development of the turbulent cascade at electron scales and the structure and dynamics of electron-scale magnetic reconnection, such as the electron diffusion region.

Key words: space plasma physics, plasma simulation, plasma waves

1. Introduction

Despite being studied with great effort for approximately a century, natural and laboratory plasmas exhibit several complex phenomena that still need to be

† Email address for correspondence: oreste.pezzi@gssi.it

https://doi.org/10.1017/S0022377819000631 Published online by Cambridge University Press

understood, mainly because of the strongly nonlinear interactions and the presence of kinetic effects. In this context, investigating plasma dynamics is decisive for understanding fundamental processes occurring in different systems, ranging from very-far astrophysical objects to the near-Earth environment and laboratory fusion devices. These systems routinely present a strongly nonlinear dynamics, which develops on a large range of spatial and time scales, including the ones associated with kinetic processes. In such systems, energy is typically injected at large fluid scales and cascades towards smaller scales, driving the system to cross three different physical regimes, ranging from fluid (magnetohydrodynamics, Hall-MHD) to ion kinetic and eventually to electron kinetic scales. This multi-scale physics is the direct consequence of the weak plasma collisionality, that characterizes solar-wind and astrophysical plasmas (Kulsrud 2005; Califano & Mangeney 2008; Bruno & Carbone 2016) as well as fusion device dynamics, where collisions can become effective at scales smaller than the electron kinetic scales (Falchetto *et al.* 2008).

As a result, the plasma is allowed to freely access the entire phase space and to manifest dynamical states far from thermal equilibrium (Galeotti & Califano 2005; Valentini *et al.* 2005; Marsch 2006; Franci *et al.* 2015; Servidio *et al.* 2015, 2017; Cerri, Kunz & Califano 2018; Franci *et al.* 2018; Pezzi *et al.* 2018; Sorriso-Valvo *et al.* 2018*b*, 2019). As an example, we highlight here the fundamental role of the collisionless magnetic reconnection, that – even within a fluid theory framework – drives a strongly nonlinear dynamics (at both ion and electron scales), without collisions being relevant (Califano, Faganello & Pegoraro 2007). Within this context, the Vlasov equation for each particle species, self-consistently coupled to Maxwell equations for the fields, provides a complete description of the system dynamics, although in some cases the role of weak collisions should be also considered (Navarro *et al.* 2016; Pezzi, Valentini & Veltri 2016; Pezzi *et al.* 2019). The Vlasov–Maxwell model is an nonlinear integro-differential set of equations in multi-dimensional phase space, whose analytic solutions are only available in a few simplified cases and in a reduced phase-space geometry. A numerical approach is therefore mandatory to describe the dynamics of collisionless magnetized plasmas in the fully nonlinear regime.

As of today, numerical simulations have provided significant insights into the plasma dynamics at proton and sub-proton spatial scales, where proton kinetic effects are dominant, while electrons can be approximated as an isothermal fluid (hybrid framework) (Valentini *et al.* 2007). In this range of scales, both particle-in-cell (PIC) and Eulerian hybrid codes have been extensively employed to investigate in detail a variety of physical phenomena such as, for instance, the development of the intermittent cascade of turbulent fluctuations (Parashar *et al.* 2009; Valentini, Califano & Veltri 2010; Servidio *et al.* 2012; Franci *et al.* 2015; Servidio *et al.* 2015; Franci *et al.* 2016; Valentini *et al.* 2016; Cerri & Califano 2017; Cerri, Servidio & Califano 2017; Valentini *et al.* 2017; Pezzi *et al.* 2017*a*,*b*; Cerri *et al.* 2018; Franci *et al.* 2018; Perrone *et al.* 2018; Sorriso-Valvo *et al.* 2018*a*), the dynamo effect in turbulent plasmas (Rincon *et al.* 2016), the interaction of solar wind and the Earth's magnetosphere at global scales (Kempf *et al.* 2013; Palmroth *et al.* 2013; Pokhotelov *et al.* 2013; Von Alfthan *et al.* 2014; Hoilijoki *et al.* 2016; Palmroth *et al.* 2018; Pfau-Kempf *et al.* 2018) and the dynamics of magnetic reconnection (Birn *et al.* 2001; Shay *et al.* 2001; Pritchett 2008; Califano *et al.* 2018). To reduce the computational cost of the simulation, reduced models – such as the gyro-kinetic (Howes *et al.* 2006, 2008*a*,*b*; Schekochihin *et al.* 2008; Tatsuno *et al.* 2009; Howes *et al.* 2011; TenBarge, Howes & Dorland 2013; Told *et al.* 2015; Howes 2016) or the finite Larmor radius

https://doi.org/10.1017/S0022377819000631 Published online by Cambridge University Press

Landau fluid ones (Passot & Sulem 2007; Sulem & Passot 2015; Sulem *et al.* 2016; Kobayashi *et al.* 2017) – have been also widely adopted to describe plasma dynamics at kinetic scales.

Within the context of space plasmas, recent high-resolution observations conducted by the magnetospheric multi-scale (MMS) mission (Burch *et al.* 2016*a*; Fuselier *et al.* 2016) allowed us, for the first time, to investigate the plasma dynamics at the electron scale. The MMS mission focuses primarily on kinetic processes occurring in the electron diffusion region of magnetic reconnection (Burch *et al.* 2016*b*; Torbert *et al.* 2016, 2018) and its unprecedented high-resolution observations confirm a very complex picture where several mechanisms can be at work in producing small-scale fluctuations (Le Contel *et al.* 2016; Breuillard *et al.* 2018; Chasapis *et al.* 2018). Magnetic reconnection often takes place within a turbulent environment where coherent structures – such as current sheets and X-points – naturally develop (Retinò *et al.* 2007; Servidio *et al.* 2009, 2010; Haggerty *et al.* 2017; Phan *et al.* 2018). At the same time, plasma jets generated by magnetic reconnection can provide energy for sustaining the turbulence itself (Cerri *et al.* 2017; Pucci *et al.* 2017, 2018). Reconnection is important for space and astrophysical plasmas as it is responsible for major plasma heating and particle acceleration in solar and stellar coronae, magnetars, accretion disks and astrophysical jets (Lyutikov 2003; Uzdensky 2011) as well as for tokamaks, being a major cause of loss of plasma confinement and plasma heating (Helander, Eriksson & Andersson 2002; Tanabe *et al.* 2015).

In order to properly combine and compare the experimental evidence at electron scales with theoretical investigations (Hesse *et al.* 2016), a huge numerical effort needs still to be made. To this end, only few numerical algorithms which retain both proton and electron kinetic physics are nowadays available. Most of them are PIC codes (Zeiler *et al.* 2002; Markidis, Lapenta & Rizwan-uddin 2010; Camporeale & Burgess 2011; Daughton *et al.* 2011; Karimabadi *et al.* 2013; Leonardis *et al.* 2013; Divin *et al.* 2015; Lapenta *et al.* 2015; Wan *et al.* 2015; Grošelj *et al.* 2017; Yang *et al.* 2017; Parashar, Matthaeus & Shay 2018; Shay *et al.* 2018; González *et al.* 2019; Lapenta *et al.* 2019), which capture the full dynamics (including electron scales) since their computational cost is smaller with respect to low-noise Eulerian (Vlasov) codes. However, at variance with noise-free Eulerian algorithms, PIC codes fail in providing a clean description of small-scale fluctuations (e.g. the electric-field behaviour around the X-point) and particle distribution functions in phase space, since they suffer from intrinsic statistical noise. Only very recently the first attempts to describe the plasma dynamics via Eulerian fully kinetic codes have become affordable, thanks to the improved supercomputer capabilities (Schmitz & Grauer 2006*a*; Umeda, Togano & Ogino 2009; Umeda *et al.* 2010; Delzanno 2015; Tronci & Camporeale 2015; Umeda & Wada 2016; Ghizzo, Sarrat & Del Sarto 2017; Umeda & Wada 2017; Juno *et al.* 2018; Roytershteyn *et al.* 2019; Skoutnev *et al.* 2019). As stated above, Eulerian algorithms generally require a computational cost significantly large as compared to PIC codes. A way to reduce the computational cost of a fully kinetic Eulerian simulation consists of applying the so-called Darwin approximation (Kaufman & Rostler 1971; Birdsall & Langdon 2004; Schmitz & Grauer 2006*a*,*b*) to the Maxwell equations based on the expansion of the Maxwell system in the small parameter v^2/c^2 (Mangeney *et al.* 2002) (v being the typical plasma bulk speed). Within this approximation, all wave modes (including those triggered by charge separation) are retained except for light waves ($v_\phi \sim c$, v_ϕ being the wave phase speed); by doing so, the numerical stability condition for the time step can be significantly relaxed.

In the present work we present a newly developed fully kinetic Eulerian Vlasov–DArwin algorithm (ViDA) which integrates numerically the kinetic equations for a

https://doi.org/10.1017/S0022377819000631 Published online by Cambridge University Press

non-relativistic globally neutral plasma composed of protons and electrons. Equations are discretized on a fixed-in-time grid in phase space with periodic boundary conditions in the physical domain. ViDA originates from the hybrid Vlasov–Maxwell code (Valentini *et al.* 2007) (hereafter referred to as the HVM code) and has been extended specifically to include electron kinetic dynamics. The paper is organized as follows. In § 2 we revisit the Darwin approximation and describe the system of equations that is numerically integrated through ViDA. We discuss in detail the strategy of the numerical integration of the Vlasov equation for each species and we show that the Darwin version of the Maxwell equations can be written as a set of Helmholtz and Poisson-like equations, solvable through a spectral method. In the same section, we also provide a description of the algorithm design. Then, in § 3 we present the first results obtained through this algorithm, concerning the propagation of (i) electrostatic Langmuir waves, (ii) whistler waves and (iii) Alfvén waves. In § 4, we describe the onset of the electron Weibel instability which is a plasma instability driven by the presence of an electron temperature anisotropy (Weibel 1959). In § 5 we present preliminary results concerning one of the main potential applications of ViDA: the magnetic reconnection process at electron scales. Then, in § 6, we discuss the performance of the algorithm. Finally, we conclude and summarize in § 7.

2. The Vlasov–Darwin (VD) model

The Darwin approximation, that we briefly revisit in the current section, has been adopted to reduce the limitations on the time steps for numerical integration (Kaufman & Rostler 1971; Mangeney *et al.* 2002; Birdsall & Langdon 2004; Schmitz & Grauer 2006*a*). Indeed, since Maxwell equations allow for the propagation of waves at the light speed c, the time step Δt of any explicit numerical scheme solving these equations would be limited by the Courant–Friedrichs–Lewy (CFL) condition, $\Delta t \lesssim \Delta x/c$ (Peyret & Taylor 1986). The Darwin approximation, by dropping the transverse displacement current term, rules out the transverse light waves (i.e. the fastest waves in the system that propagate at phase speed c) and significantly relaxes the CFL condition.

We consider a non-relativistic, collisionless, fully kinetic plasma composed of electrons and protons. The Vlasov–Darwin system of equations reads (in CGS units),

$$\partial_t f_\alpha + \boldsymbol{v}\cdot\boldsymbol{\nabla} f_\alpha + \frac{Z_\alpha e}{m_\alpha}\left(\boldsymbol{E} + \frac{\boldsymbol{v}}{c}\times\boldsymbol{B}\right)\cdot\boldsymbol{\nabla}_{\boldsymbol{v}} f_\alpha = 0, \tag{2.1}$$

$$\boldsymbol{\nabla}\cdot\boldsymbol{E}_L = 4\pi\rho_c, \tag{2.2}$$

$$\boldsymbol{\nabla}\cdot\boldsymbol{B} = 0, \tag{2.3}$$

$$\boldsymbol{\nabla}\times\boldsymbol{E}_T = -\frac{1}{c}\partial_t\boldsymbol{B}, \tag{2.4}$$

$$\boldsymbol{\nabla}\times\boldsymbol{B} = \frac{1}{c}\partial_t\boldsymbol{E}_L + \frac{4\pi}{c}\boldsymbol{j}, \tag{2.5}$$

where $f_\alpha(\boldsymbol{x}, \boldsymbol{v}, t)$ is the distribution function (DF) of the $\alpha = p, e$ species, m_α and Z_α are respectively the mass and charge number of the α species and c is the light speed; ∂_t, $\boldsymbol{\nabla}$ and $\boldsymbol{\nabla}_{\boldsymbol{v}}$ indicate the derivatives with respect to the time t, the spatial coordinates $\boldsymbol{x}$ and the velocity coordinates $\boldsymbol{v}$, respectively; $\boldsymbol{E}(\boldsymbol{x}, t) = \boldsymbol{E}_L(\boldsymbol{x}, t) + \boldsymbol{E}_T(\boldsymbol{x}, t)$ and $\boldsymbol{B}(\boldsymbol{x}, t)$ are the electric and magnetic field, respectively. The electric field has been decomposed into a longitudinal (irrotational, $\boldsymbol{\nabla}\times\boldsymbol{E}_L = 0$) and a transverse (solenoidal, $\boldsymbol{\nabla}\cdot\boldsymbol{E}_T = 0$) component (Griffiths 1962). According to the Darwin approximation, the transverse

https://doi.org/10.1017/S0022377819000631 Published online by Cambridge University Press

component of the displacement current has been neglected in Ampere's law (2.5) (Birdsall & Langdon 2004; Schmitz & Grauer 2006*a*). The Darwin model, that retains at least the longitudinal component of the displacement current, is generally closer to the full Maxwell system with respect to models where the displacement current is completely neglected (Valentini *et al.* 2007; Tronci & Camporeale 2015).

The plasma charge density $\rho_c(\boldsymbol{x}, t)$ and the current density $\boldsymbol{j}(\boldsymbol{x}, t)$ are defined through the first two velocity moments of the particle DFs,

$$\rho_c = e\sum_\alpha Z_\alpha n_\alpha = e\sum_\alpha Z_\alpha \int \mathrm{d}\boldsymbol{v} f_\alpha, \tag{2.6}$$

$$\boldsymbol{j} = \sum_\alpha \boldsymbol{j}_\alpha = e\sum_\alpha Z_\alpha n_\alpha V_\alpha = e\sum_\alpha Z_\alpha \int \mathrm{d}\boldsymbol{v}\boldsymbol{v} f_\alpha. \tag{2.7}$$

Equations (2.1)–(2.5) can be further simplified to obtain a set of Helmholtz-like equations of state without explicit time derivatives (see Birdsall & Langdon (2004) and Schmitz & Grauer (2006*a*) for details). By normalizing equations using a characteristic length $\bar{L}$, time $\bar{t}$, velocity $\bar{U} = \bar{L}/\bar{t}$, mass $\bar{m}$ and distribution function $f_{\alpha,0} = \bar{n}/\bar{U}^3$ (with $\bar{n} = \bar{L}^{-3}$ the equilibrium density), it is straightforward to get the dimensionless Vlasov–Darwin system of equations,

$$\partial_t f_\alpha + (\boldsymbol{v}\cdot\nabla) f_\alpha + \frac{Z_\alpha}{\mu_\alpha}(\boldsymbol{E} + \boldsymbol{v}\times\boldsymbol{B})\cdot\nabla_v f_\alpha = 0, \tag{2.8}$$

$$\nabla^2\varphi = -\zeta^2\sum Z_\alpha n_\alpha, \quad \boldsymbol{E}_L = -\nabla\phi, \tag{2.9a,b}$$

$$\nabla^2\boldsymbol{B} = -\bar{u}^2\zeta^2\nabla\times\boldsymbol{j}, \tag{2.10}$$

$$\nabla^2\hat{\boldsymbol{E}}_T - \bar{u}^2\zeta^2\sum_\alpha \frac{Z_\alpha^2 n_{\alpha,0}}{\mu_\alpha}\hat{\boldsymbol{E}}_T = \bar{u}^2\zeta^2\left[-\nabla\cdot\sum_\alpha Z_\alpha\langle\boldsymbol{v}\boldsymbol{v}\rangle_\alpha + \sum_\alpha \frac{Z_\alpha^2}{\mu_\alpha}(n_\alpha\boldsymbol{E}_L + \langle\boldsymbol{v}\rangle_\alpha\times\boldsymbol{B})\right], \tag{2.11}$$

$$\nabla^2\Theta = \nabla\cdot\hat{\boldsymbol{E}}_T, \quad \boldsymbol{E}_T = \hat{\boldsymbol{E}}_T - \nabla\Theta, \tag{2.12a,b}$$

$$\nabla\cdot\boldsymbol{B} = 0, \tag{2.13}$$

where $\langle h\rangle_\alpha = \int \mathrm{d}\boldsymbol{v} f_\alpha h$. In (2.8)–(2.13), the electric and magnetic fields are normalized to $\bar{E} = \bar{m}\bar{U}/e\bar{t}$ and $\bar{B} = \bar{m}c/e\bar{t}$, respectively. Note also that we set $k_B = 1$. Non-dimensional parameters are $\mu_\alpha = m_\alpha/\bar{m}$, $\bar{u} = \bar{U}/c$ and $\zeta = \bar{\omega}_p\bar{t}$, with $\bar{\omega}_p = \sqrt{4\pi e^2\bar{n}/\bar{m}}$. Note that in (2.11) we have omitted a term $\bar{u}^2\nabla\partial_{tt}\phi$ which could generate, in principle, an irrotational component, and we have introduced (2.12*a*,*b*) to preserve the solenoidality of $\boldsymbol{E}_T$ (Schmitz & Grauer 2006*a*). The spatial dependence of n_α on the left-hand side of (2.11) has been neglected ($n_\alpha \simeq n_{\alpha,0}$) to let the coefficients be constant (Valentini *et al.* 2007).

2.1. *Conservation properties*

It is straightforward to verify that (2.8)–(2.13) satisfy mass $\int \mathrm{d}\boldsymbol{x}\,\mathrm{d}\boldsymbol{v} f_\alpha$ and entropy $S_\alpha = \int \mathrm{d}\boldsymbol{x}\,\mathrm{d}\boldsymbol{v} f_\alpha \log f_\alpha$ conservation. The energy conservation equation, obtained by

https://doi.org/10.1017/S0022377819000631 Published online by Cambridge University Press

multiplying (2.8) by $m_\alpha \boldsymbol{v}^2/2$, integrating over the phase-space volume $\int \mathrm{d}\boldsymbol{x}\,\mathrm{d}\boldsymbol{v}$ and summing over the species reads,

$$\mathcal{E}_{\mathrm{kin}} + \mathcal{E}_{\mathrm{th}} + \mathcal{E}_{\mathrm{mag}} + \mathcal{E}_{\mathrm{el}} = \mathrm{const.}, \tag{2.14}$$

where the kinetic energy is $\mathcal{E}_{\mathrm{kin}} = \sum_\alpha (m_\alpha/2)\int \mathrm{d}\boldsymbol{x} n_\alpha \boldsymbol{u}_\alpha^2$, the thermal energy is $\mathcal{E}_{\mathrm{th}} = \sum_\alpha (3/2)\int \mathrm{d}\boldsymbol{x} n_\alpha T_\alpha$, the magnetic energy is $\mathcal{E}_{\mathrm{mag}} = \sum_\alpha (\bar{m}/2\bar{u}^2\zeta^2)\int \mathrm{d}\boldsymbol{x}\boldsymbol{B}^2$ and the electrostatic energy is $\mathcal{E}_{\mathrm{el}} = \sum_\alpha (\bar{m}/2\zeta^2)\int \mathrm{d}\boldsymbol{x}\boldsymbol{E}_L^2$. Note that the temperature of the α-species is defined as $3n_\alpha T_\alpha/m_\alpha = \int \mathrm{d}\boldsymbol{v}(\boldsymbol{v} - \boldsymbol{u}_\alpha)^2 f_\alpha$ and, to get (2.14), we have used $\int \mathrm{d}\boldsymbol{x}\boldsymbol{w}_T \cdot \boldsymbol{w}_L = 0$, $\boldsymbol{w}_T$ and $\boldsymbol{w}_L$ being a generic transverse and longitudinal vector, respectively. In each of the tests described in the present work we have checked the conservation of these quantities: their variation with respect to initial values is always smaller than the 1 %.

2.2. *ViDA algorithm and code design*

The Vlasov equation for each species is integrated numerically by employing the time splitting method first proposed by Cheng & Knorr (1976) in the electrostatic limit and later extended to the full electromagnetic case (Mangeney *et al.* 2002). Darwin equations are solved through standard fast Fourier transform (FFT) algorithms.

In our case, the splitting algorithm for (2.8) reads as follows:

$$\partial_t f_\alpha + (\boldsymbol{v}\cdot\nabla) f_\alpha = 0 \tag{2.15}$$

$$\partial_t f_\alpha + \frac{Z_\alpha}{\mu_\alpha}(\boldsymbol{E} + \boldsymbol{v}\times\boldsymbol{B})\cdot\nabla_v f_\alpha = 0. \tag{2.16}$$

In the first equation $\boldsymbol{v}$ is a parameter, while in the second equation $\boldsymbol{x}$, $\boldsymbol{E}$ and $\boldsymbol{B}$ are parameters. At time t, the solutions of (2.15)–(2.16) can be written as $\Lambda_{\boldsymbol{x}}(t)F_\alpha(\boldsymbol{x},\boldsymbol{v})$ and $\Lambda_{\boldsymbol{v}}F_\alpha(\boldsymbol{x},\boldsymbol{v})$, respectively. In last expressions, $\Lambda_{\boldsymbol{x}}$ and $\Lambda_{\boldsymbol{v}}$ are the advection operators in physical and velocity space, whose explicit definition, based on the third-order van Leer scheme, can be found in Mangeney *et al.* (2002); while $F_\alpha(\boldsymbol{x},\boldsymbol{v}) = f_\alpha(\boldsymbol{x},\boldsymbol{v},t=0)$ is the initial condition. Note that $\Lambda_{\boldsymbol{v}}$ depends also on the particle species α and, for the sake of simplicity, we avoid to explicitly report such dependence.

The splitting scheme is a symplectic, second order accurate in time (see Mangeney *et al.* (2002) where the stability condition of the advection operator is also discussed) and the numerical solution at $t = t_N = N\Delta t$ is given by,

$$f_\alpha(\boldsymbol{x},\boldsymbol{v},t_N) = \left[\Lambda_{\boldsymbol{x}}\left(\frac{\Delta t}{2}\right)\Lambda_{\boldsymbol{v}}(\Delta t)\Lambda_{\boldsymbol{x}}\left(\frac{\Delta t}{2}\right)\right]^N f_\alpha(\boldsymbol{x},\boldsymbol{v},0). \tag{2.17}$$

At $t=0$, the distribution function $F_\alpha(\boldsymbol{x},\boldsymbol{v}) = f_\alpha(\boldsymbol{x},\boldsymbol{v},t=0)$ is first advected in physical space by half of a time step, obtaining $\tilde{f}_\alpha(\boldsymbol{x},\boldsymbol{v},\Delta t/2)$. Then, the following structure is executed:

(i) computing the moments of $\tilde{f}_\alpha$ and evaluating the electromagnetic fields $\boldsymbol{E}_L$, $\boldsymbol{E}_T$ and $\boldsymbol{B}$, at $t = \Delta t/2$, through (2.9*a*,*b*)–(2.13);

(ii) performing a time-step advection in velocity space: $\hat{f}_\alpha = \Lambda_{\boldsymbol{v}}(\Delta t)\tilde{f}_\alpha$;

(iii) performing a time-step advection in physical space: $\tilde{f}_\alpha = \Lambda_{\boldsymbol{x}}(\Delta t)\hat{f}_\alpha$.

https://doi.org/10.1017/S0022377819000631 Published online by Cambridge University Press

This last structure is repeated in the algorithm, according to (2.17), in order to get the evolved distribution function at any time instant.

The phase-space domain is discretized as follows. The physical space $D_{\boldsymbol{x}} = [0, L_x] \times [0, L_y] \times [0, L_z]$ is discretized with $N_x \times N_y \times N_z$ gridpoints and periodic boundary conditions are used. The velocity space $D_{\boldsymbol{v},\alpha} = [-v_{\alpha,x}^{\max}, v_{\alpha,x}^{\max}] \times [v_{\alpha,y}^{\max}, v_{\alpha,y}^{\max}] \times [-v_{\alpha,z}^{\max}, v_{\alpha,z}^{\max}]$ is discretized by $(2N_{\alpha,v_x} + 1) \times (2N_{\alpha,v_y} + 1) \times (2N_{\alpha,v_z} + 1)$ grid points. Velocity-space boundary conditions impose $f_\alpha(|v_i| > v_{\alpha,i}^{\max}) = 0$ $(i = x, y, z)$. In order to ensure mass conservation, $v_{\alpha,i}^{\max}$ is typically set to be a large multiple of the thermal speed $v_{\mathrm{th},\alpha} = \sqrt{T_\alpha/m_\alpha}$.

The ViDA algorithm has been designed in such a way that the user can select (i) different normalizations of the model equations, (ii) the possibility of setting motionless protons and (iii) different dimensionalities of the physical-space domain (one, two or three dimensions), the velocity-space domain being always three-dimensional ($3V$). Within ViDA spatial vectors always have three components and can be function of one, two or three spatial variables, depending on the physical-space dimensionality. Since Darwin equations are a set of Helmholtz-like equations, initial perturbations have to be introduced through the particle DFs (and their moments): this represents a difference with respect to standard codes where also magnetic perturbations can be introduced. A check on the solenoidality of $\boldsymbol{B}$ and $\boldsymbol{E}_T$ is also implemented at each time step.

The computational effort necessary to solve VD equations is significant and a massive parallelization, based on both MPI and OpenMP paradigms is implemented. The MPI paradigm, first introduced for the DF by Mangeney *et al.* (2002), is adopted to parallelize the physical-space computational domain for both particle DFs (and their moments) and electromagnetic field. Hence each MPI thread accesses a finite portion of phase space, composed by a sub-portion of physical space and by the whole velocity space. Within each MPI thread, the OpenMP directives are adopted to parallelize the velocity-space cycles. The parallelization of the electromagnetic field is a new feature recently introduced in the HVM code in Cerri & Califano (2017) and it is essential to perform high-resolution Eulerian Vlasov simulations, in particular in three dimensions. Preliminary tests on performance and scalability are reported in § 6.

2.3. *Normalizations of the Vlasov–Darwin equations*

In order to normalize (2.8)–(2.13), three possible choices have been implemented in ViDA:

(i) Electrostatic normalization. Characteristic quantities are: length $\bar{L} = \lambda_{D,e}$, time $\bar{t} = \omega_{p,e}^{-1}$, velocity $\bar{U} = v_{\mathrm{th},e}$ and mass $\bar{m} = m_e$. Here $\lambda_{D,e} = \sqrt{T_e/4\pi n_e e^2}$, $\omega_{p,e} = (\sqrt{4\pi n_e e^2/m_e})^{-1}$, $v_{\mathrm{th},e} = \sqrt{T_e/m_e} = \lambda_{D,e}\omega_{p,e}$ and m_e are the electron Debye length, the electron plasma frequency, the electron thermal speed and the electron mass, respectively. This normalization is appropriate for describing phenomena occurring at electron scales, such as the propagation of electrostatic plasma waves.

(ii) Electromagnetic normalization. Characteristic quantities are: length $\bar{L} = d_e$, time $\bar{t} = \omega_{p,e}^{-1}$, velocity $\bar{U} = c$ and mass $\bar{m} = m_e$, where $d_e = c/\omega_{p,e}$ is the electron skin depth. This normalization can be adopted for describing electromagnetic phenomena, where both protons and electrons are involved, such as magnetic reconnection and plasma turbulence at kinetic scales.

https://doi.org/10.1017/S0022377819000631 Published online by Cambridge University Press

(iii) Hybrid normalization. Characteristic quantities are: length $\bar{L} = d_p$, time $\bar{t} = \Omega_{c,p}^{-1}$, velocity $\bar{U} = v_A$ and mass $\bar{m} = m_p$. In previous expressions $\Omega_{cp} = eB_0/m_p c$, $v_A = B_0/\sqrt{4\pi n_p m_p}$, $d_p = v_A/\Omega_{cp}$ and m_p are the proton cyclotron frequency, the proton Alfvén speed, the proton skin depth and the proton mass, respectively. This normalization is useful for investigating the turbulent cascade in the sub-proton range, where electron physics starts to play a role.

These three normalizations can be adopted to describe, in a more natural way (i.e. characteristic scales close to unity), phenomena where electrostatic, electromagnetic or proton inertial effects dominate, respectively.

3. Numerical tests of ViDA

In this section we report the results of several tests performed to evaluate the capabilities of ViDA in describing basic collisionless plasma physics dynamics. The proper behaviour and reliability of the code have been tested against the propagation of Langmuir waves, in both linear and nonlinear regimes, whistler waves and Alfvén waves.

3.1. *Propagation and damping of Langmuir waves*

For these tests we adopted the electrostatic normalization. We discuss results of simulations performed with motionless protons in 1D–3V phase-space configuration, where Langmuir waves propagate along the x direction. Physical and velocity space have been discretized with $N_x = 128$ and $N_{e,v_x} = 50$, $N_{e,v_y} = N_{e,v_z} = 15$ grid points, respectively. In the case of mobile protons ($m_p/m_e = 1836$ and $T_p/T_e = 1$), the propagation of Langmuir waves has been reproduced with lower phase-space resolution, but the results are quantitatively similar to those discussed in the following. We have also separately tested the propagation of Langmuir waves along y and z directions by carrying out 2D–3V and 3D–3V runs.

The initial equilibrium is given by an electron Maxwellian distribution spatially homogeneous. The plasma is unmagnetized, the initial electron temperature is $T_e = 1$ (in scaled units). At $t = 0$, the electron number density is perturbed through a sinusoidal perturbation $\delta n_e/n_{e,0} = A\sin(kx)$, $A = 10^{-4}$ and $k = k_1 = 2\pi/L$ being the amplitude and the wavenumber, respectively. The box length is $L = 18\lambda_{D,e}$ ($k_1 = 0.35$) and $v_{e,i}^{\max} = 5v_{\mathrm{th},e}$ ($i = x, y, z$). The system evolution is reproduced up to a maximum time $t_{\max} = 100\omega_{p,e}^{-1}$, while the numerical recurrence time is $t_{\mathrm{rec}} = 2\pi/k\Delta v \simeq 180\omega_{p,e}^{-1}$ (Cheng & Knorr 1976; Galeotti, Califano & Pegoraro 2006; Pezzi *et al.* 2016).

Figure 1(*a*) shows the time evolution of the amplitude of the $k_x = k_1$ Fourier component of the electric field $|E_x|(k_1, t)$, in a semi-logarithmic plot. The electric field undergoes Landau damping (Landau 1946); the observed damping rate shows a very good agreement with the theoretical prediction $\gamma_L = -3.37 \times 10^{-2}\omega_{p,e}$ (red-dashed line), evaluated through a numerical linear solver for the roots of the electrostatic Vlasov dielectric function. In figure 1(*b*) we report the resonant curve, obtained by Fourier transforming the electric signal in space and time; we plot the spectral electric energy $|E_x|^2(k_1, \omega_R)$ as a function of the pulsation ω_R. As expected, the resonant curve displays a well-defined frequency peak in correspondence of a value of the pulsation $\omega_R = 1.22\omega_{p,e}$. In figure 1(*b*), the vertical red-dashed line represents the value of the theoretical resonant pulsation $\omega_{R,\mathrm{th}}$ obtained through the linear solver, while the two vertical red-dot-dashed lines indicate the interval of uncertainty of the numerical code,

https://doi.org/10.1017/S0022377819000631 Published online by Cambridge University Press

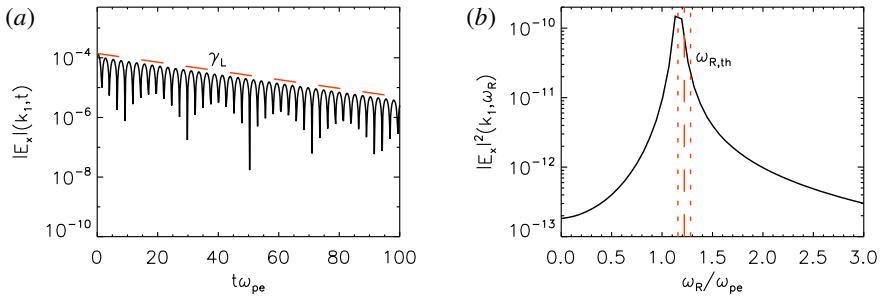


FIGURE 1. (*a*) Time evolution of $|E_x|(k_1, t)$. The red dashed line indicates the predicted Landau damping rate γ_L. (*b*) Energy peak $|E_x|^2(k_1, \omega_R)$ as a function of the pulsation ω_R. The red dashed line indicates the theoretical wave frequency $\omega_{R,\mathrm{th}}$, while red dot-dashed lines show the ω_R – resolution, i.e. $\omega_{R,\mathrm{th}} \pm \Delta\omega_R/2$. The theoretical expectations for the Langmuir wave damping and the pulsation have been obtained with a numerical solver of the linear dispersion relation.

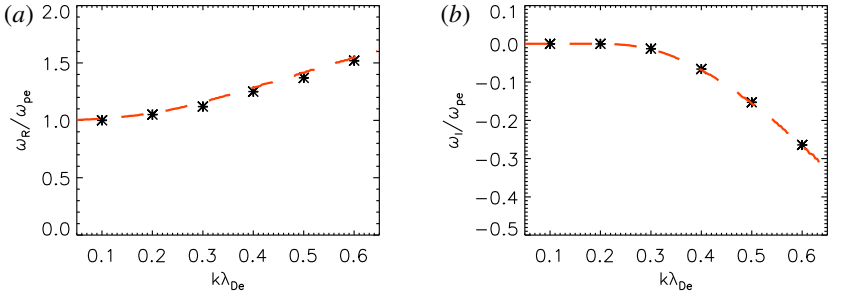


FIGURE 2. Pulsation ω_R (*a*) and damping rate γ_I (*b*), in units of $\omega_{p,e}$, from the simulation (black dots) and from the linear numerical solver (red dashed line) as a function of the wavenumber $k\lambda_{D,e}$.

due to the time discretization $\Delta\omega_R = 2\pi/t_{\max} \simeq 0.063\omega_{p,e}$. Again, numerical results are in very good agreement with theoretical predictions.

In order to show the dependence of the real ω_R and imaginary ω_I parts of the frequency as a function of the wavenumber, we have performed an additional $1D$–$3V$ run, in which the initial perturbation is a superposition of the first six wavenumbers $k_x = [k_1, 6k_1]$, where $k_1 = 2\pi/L$ ($L = 2\pi 10\lambda_{D,e}$); the other parameters are the same as in the previous run. To avoid numerical recurrence, phase space has been discretized with $N_x = 128$, $N_{e,v_x} = 100$ and $N_{e,v_y} = N_{e,v_z} = 15$. Figure 2 reports by stars the dependence of ω_R (*a*) and ω_I (*b*), in units of ω_{pe}, as a function of the wavenumber $k\lambda_{D,e}$. A very good agreement with theoretical expectations (red-dashed curves) is recovered for both real and imaginary parts of the complex frequency.

We conclude this section by focusing on the nonlinear regime of the Langmuir wave dynamics (see, for example, Brunetti, Califano & Pegoraro (2000) and references therein). We have performed ten different runs, varying the amplitude of the initial density perturbation in the range $A = [8 \times 10^{-3}, 8 \times 10^{-2}]$. In this case, phase space has been discretized with $N_x = 128$, $N_{e,v_x} = 150$ and $N_{e,v_y} = N_{e,v_z} = 15$, while $t_{\max} = 400\omega_{pe}^{-1}$. The box length is $L_x = 18\lambda_{D,e}$, while $v_{e,i}^{\max} = 5v_{\mathrm{th},e}$ ($i = x, y, z$). As reported in figure 3(*a*), the time evolution of the electric-field Fourier component shows an

https://doi.org/10.1017/S0022377819000631 Published online by Cambridge University Press

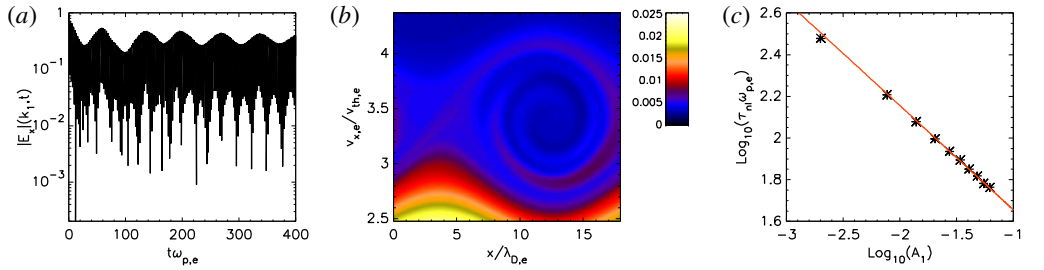


FIGURE 3. (*a*) Time evolution of $|E_x(k_1, t)|$ for the simulation with $A = 8 \times 10^{-2}$. (*b*) Contour plot of $\tilde{f}_e(x, v_x) = \int \mathrm{d}v_y\, \mathrm{d}v_z f_e(x, \boldsymbol{v})$ in the plan x–v_x. (*c*) Nonlinear time τ_{nl} as a function of the first peak amplitude A_1. The red line reports the predicted scaling ~ -0.5 (the result of the linear fit is ~ -0.48).

early linear damping phase (Landau 1946), until particle trapping arrests the damping and produces oscillations of the signal envelope (O'Neil 1965). At large times, a phase-space vortex is observed in the electron DF in the vicinity of the wave phase speed, as reported in figure 3(*b*). As it has been shown in O'Neil (1965), the nonlinear trapping time τ_{nl} depends on the saturation amplitude A_1 of the electric oscillations as $\tau_{\mathrm{nl}} \sim A_1^{-1/2}$. For each of the ten simulations, we evaluated A_1 and τ_{nl} at the time of the first peak of the electric envelope oscillations. Figure 3(*c*) shows in log–log plot τ_{nl} as a function of A_1 (stars), compared to the theoretical expectation (red line), showing a very nice agreement.

3.2. *Propagation of whistler waves*

To reproduce the propagation of whistler waves at electron scales, the electromagnetic normalization has been employed. Protons are assumed just as a fixed neutralizing background. Again, we have verified that the ViDA code behaves exactly in the same manner in the three spatial directions. Hence, we discuss here the result of a $1D$–$3V$ run, where $\boldsymbol{B}_0 = B_0 \boldsymbol{e}_x$ ($B_0 = 1$) and protons are not fixed. The box length is $L_x = 2\pi 10 d_e$, while $v_{e,i}^{\max} = 10 v_{\mathrm{th},e}$ and $v_{p,i}^{\max} = 7 v_{\mathrm{th},p}$ ($i = x, y, z$). Note that increasing the value of $v_{p(e)}^{\max}$ has been necessary to ensure mass conservation. The phase space has been discretized with $N_x = 128$, $N_{e,v_x} = N_{e,v_y} = N_{e,v_z} = 50$ and $N_{p,v_x} = N_{p,v_y} = N_{p,v_z} = 35$. We also set $m_p/m_e = 1836$, $T_e/T_p = 1$, $\bar{u} = v_{\mathrm{th},e}/c = 10^{-3}$ and $\zeta = 1$.

The equilibrium is composed of Maxwellian velocity distributions for both protons and electrons and homogeneous density. The initial equilibrium is then perturbed with the following electron bulk-speed perturbations:

$$\delta u_{e,y} = A \sin(kx), \tag{3.1}$$

$$\delta u_{e,z} = A \cos(kx), \tag{3.2}$$

where $A = 10^{-3}$ and $k = k_1 = 2\pi/L_x$.

By solving the Darwin equations, these perturbations generate a current density and then magnetic fluctuations. Figure 4 reports the time evolution of $|B_y|(k_1, t)$ (*a*) and the frequency peak of the spectral magnetic energy $|B_y|^2(k_1, \omega_R)$ as a function of the pulsation ω_R (*b*). The magnetic field clearly oscillates at the correct frequency $\omega_{R,\mathrm{th}} = 0.91\omega_{p,e}$, that can be evaluated from the linear dispersion relation for whistler waves (obtained by assuming motionless protons and cold electrons): $\omega_{R,\mathrm{th}}(k) = B_0 k^2/(1 + k^2)$

https://doi.org/10.1017/S0022377819000631 Published online by Cambridge University Press

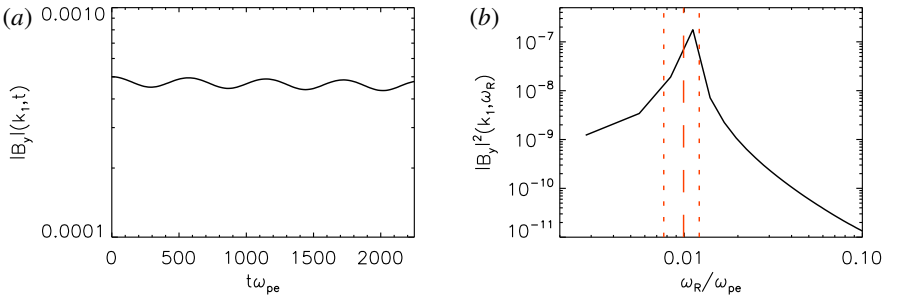


FIGURE 4. (*a*) Time evolution of $|B_y|(k_1, t)$. (*b*) Spectral magnetic energy $|B_y|^2(k_1, \omega_R)$ as a function of the pulsation ω_R. The red dashed line indicates the theoretical wave frequency $= \omega_{R,\mathrm{th}}$, while the red dot-dashed lines show the ω_R-resolution $\omega_{R,\mathrm{th}} \pm \Delta\omega_R/2$.

(Krall & Trivelpiece 1973). Note that, for the considered wavenumber, a negligible damping of whistler waves is expected. In figure 4(*a*), the red-dashed line represents the value of the resonant pulsation from the above expression for $\omega_{R,\mathrm{th}}$, while the two vertical red dot-dashed lines indicate the interval of numerical uncertainty $\Delta\omega_R = 2\pi/t_{\max} \simeq 0.063\omega_{p,e}$.

3.3. *Propagation of Alfvén waves*

Here we show numerical results concerning the propagation of Alfvén waves along a background magnetic field. The adopted normalization for these tests is the hybrid one. We perform a 1*D*–3*V* run, where $\boldsymbol{B}_0 = B_0\boldsymbol{e}_x$ and $B_0 = 1$. The box length is $L_x = 2\pi 50 d_p$, while $v_{e,i}^{\max} = 5v_{\mathrm{th},e}$ and $v_{p,i}^{\max} = 5v_{\mathrm{th},p}$ $(i = x, y, z)$. The phase space has been discretized with $N_x = 32$, $N_{e,v_x} = N_{e,v_y} = N_{e,v_z} = 25$, $N_{p,v_x} = 40$ and $N_{p,v_y} = N_{p,v_z} = 35$ gridpoints. The mass ratio has been artificially set to $m_p/m_e = 25$, thus avoiding extremely small time steps, while $T_e/T_p = 1$, $\bar{u} = v_A/c = 10^{-3}$, $\zeta = c/v_A = 10^3$ and $\beta_p = 2v_{\mathrm{th},p}^2/v_A^2 = 1$.

The initial equilibrium, composed of spatially homogeneous Maxwellian protons and electrons, has been perturbed with the following proton bulk-speed perturbations:

$$\delta u_{p,y} = A\sin(kx), \tag{3.3}$$

$$\delta u_{p,z} = A\cos(kx), \tag{3.4}$$

where $A = 10^{-4}$ and $k = k_1 = 2\pi/L_x$. Figure 5 shows the time evolution of $|B_z|(k_1, t)$ (*a*) and the magnetic spectral energy $|B_z|^2(k_1, \omega_R)$ as a function of ω_R (*b*). The recovered resonant peak is in agreement with the theoretical pulsation, evaluated through a fully kinetic linear solver of the dispersion relation (Camporeale & Burgess 2017). Moreover, no Landau damping is observed, since it occurs at much smaller scales (Barnes 1966; Vàsconez *et al.* 2014; Camporeale & Burgess 2017). This test represents the first attempt towards a general description of Alfvén waves, where electron physics is also taken into account. Since including electron physics is currently too computational demanding, we plan to continue the investigation in a separate, future work.

4. Temperature anisotropy driven instability: electron Weibel instability

Another class of interesting numerical tests, which can be performed to point out the reliability of the ViDA code, concerns the onset of micro-instabilities, such as whistler,

https://doi.org/10.1017/S0022377819000631 Published online by Cambridge University Press

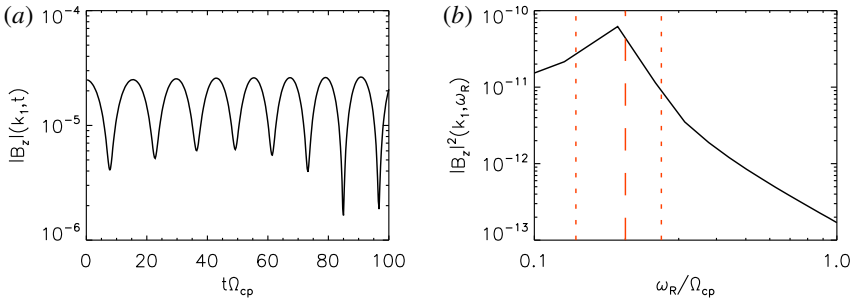


FIGURE 5. (*a*) Time evolution of $|B_z|(k_1, t)$. (*b*) Magnetic spectral energy $|B_z|^2(k_1, \omega_R)$ as a function of ω_R. The red solid line indicates the theoretical wave frequency $\omega_{R,\mathrm{th}}$, while red dashed lines show the ω_R-resolution $\omega_{R,\mathrm{th}} \pm \Delta\omega_R/2$.

mirror and Weibel instabilities driven by a temperature anisotropy (Weibel 1959; Gary & Karimabadi 2006; Califano *et al.* 2008; Palodhi, Califano & Pegoraro 2009, 2010; Chen & Chacón 2014; Camporeale & Zimbardo 2015; Chen & Chacón 2015).

Here we focus on the development of the electron Weibel instability, that produces electromagnetic fluctuations transverse to the wavevector $\boldsymbol{k}$. The most suitable normalization to perform this analysis is the electromagnetic one. In particular we discuss the results of a 1D–3V run with $\boldsymbol{k} = k\hat{\boldsymbol{e}}_x$, although we have verified that instability is triggered in the same way also in the different phase-space configuration (two and three dimensions). The mass ratio is $m_p/m_e = 100$, while $T_e/T_p = 0.01$. Electrons are initialized with a bi-Maxwellian distribution function, with thermal speeds $v_{\mathrm{th},e,x} = 2.5 \times 10^{-2}c$ and $v_{\mathrm{th},e,y} = v_{\mathrm{th},e,z} = 4 \times 10^{-2}c$, this giving a temperature anisotropy $A = T_{y(z)}/T_x = 2.56$. Protons have a Maxwellian velocity distribution at $t = 0$, with a thermal speed $v_{\mathrm{th},p} = v_{\mathrm{th},e,x}$ and homogeneous density. However, in this case, protons mainly act just as a neutralizing background, not being involved in the dynamics during the linear stage (i.e. during the instability development). No background magnetic field has been introduced. Physical space, whose length is $L_x = 32d_e$, has been discretized with $N_x = 64$ gridpoints. Velocity space has been discretized with 51^3 gridpoints for both protons and electrons and $v_{e(p)}^{\max} = 5v_{\mathrm{th},e(p)}$ in each velocity directions.

The initial equilibrium has been perturbed through a sinusoidal, transverse perturbation, imposed on the electron bulk speed,

$$\delta u_{e,y} = A\sin(kx), \tag{4.1}$$

$$\delta u_{e,z} = A\cos(kx), \tag{4.2}$$

where $A = 2 \times 10^{-5}$ and $k = k_1 = 2\pi/L_x$. Such bulk-speed perturbations produce a current density, which in turn generates magnetic fluctuations. Figure 6 reports the time evolution of the magnetic spectral energy density $W_B(k_1, t) = (|B_y|^2(k_1, t) + |B_z|^2(k_1, t))/2$. The red-dashed line indicates the expected linear instability growth rate $\omega_I^{\mathrm{th}} \simeq 4 \times 10^{-3}\omega_{p,e}$, evaluated through a linear solver for the roots of the kinetic electromagnetic dielectric function. In the early stage of the simulation, W_B increases exponentially with a growth rate in very good agreement with the expected one. Then, oscillations saturate at a nearly constant value in the nonlinear regime of evolution (Chen & Chacón 2014).

https://doi.org/10.1017/S0022377819000631 Published online by Cambridge University Press

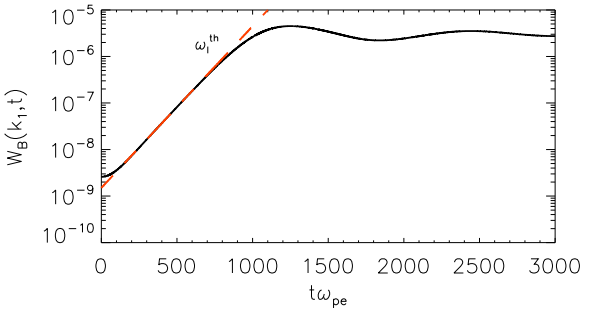


FIGURE 6. Time evolution of $W_B(k_1) = (|B_y|^2(k_1) + |B_z|^2(k_1))/2$. The red dashed line indicates the linear instability growth $\omega_I^{\rm th} \simeq 4 \times 10^{-3}\omega_{p,e}$, calculated with a linear solver of the fully kinetic dispersion relation (Camporeale & Burgess 2017).

5. Dynamics of magnetic reconnection

In this section we present the results of a magnetic reconnection simulation. Generally speaking, Vlasov simulations of magnetic reconnection represent a strong numerical challenge because of the huge memory and CPU time required by Eulerian algorithms. This approach, if successful, would certainly provide a crucial contribution to the understanding of the magnetic reconnection process especially at electron scales, thanks to the fact that Eulerian algorithms allow for an almost noise-free description of fields and particle DFs. A noise-free description is crucial to properly understand e.g. which electromagnetic fluctuations contribute to the reconnection electric field in the form of anomalous resistivity and how distribution functions are modified leading to electron heating.

We have performed a $2D$–$3V$ symmetric magnetic reconnection simulation. Reconnection is symmetric when the values of magnetic field and density are equal on the two opposite sides of the current sheet. The initial condition of our simulation is the one adopted in the geospace environmental modeling (GEM) challenge (Birn *et al.* 2001), in order to allow for a direct comparison to previous studies (Birn *et al.* 2001; Schmitz & Grauer 2006*b*). For this reason, we have also chosen the hybrid normalization (see § 2.3).

The equilibrium is set by adapting the Harris equilibrium (Harris 1962) to the periodic boundary conditions in the spatial domain. In particular, the component of the magnetic field $B_x(y)$ corresponding to the double current sheet profile reads,

$$B_x(y) = B_0 \left[\tanh\left(\frac{y - L_y/2}{L_1}\right) - \tanh\left(\frac{y}{L_2}\right) - \tanh\left(\frac{y - L_y}{L_2}\right) \right]. \tag{5.1}$$

This profile is characterized by the presence of two gradients (the current sheets) varying as an hyperbolic tangent and located at $y = L_y/2$ and $y = 0$ (and so at $y = L_y$) where L_y is the length of the spatial domain in the y direction. The first hyperbolic tangent is the one defined in Harris (1962) and L_1 is the corresponding current sheet thickness. The second and third hyperbolic tangents in (5.1) have been included to satisfy the spatial periodicity; the value of L_2 is taken sufficiently large compared to L_1 to slow down the development of reconnection in the second current sheet with respect to the main one. The electron and ion temperature are set as uniform at the initial time and the density $n(y)$ is defined in order to satisfy pressure balance. Then, from (2.5)

https://doi.org/10.1017/S0022377819000631 Published online by Cambridge University Press

and considering $\partial_t \boldsymbol{E}_L = 0$ at the initial time, we get the initial current density $\boldsymbol{j} = (0, 0, j_z(y))$.

Following the prescriptions of the Harris equilibrium we get, in normalized units,

$$n_0(T_e + T_p) = \frac{B_0^2}{2}, \tag{5.2}$$

$$\frac{u_{e,0}}{T_e} = -\frac{u_{p,0}}{T_p}, \tag{5.3}$$

$$\frac{j_z(y)}{n(y)} \equiv u_0 = u_{p,0} - u_{e,0}. \tag{5.4}$$

Equation (5.3) corresponds to the no charge separation condition of the Harris equilibrium so that quasi-neutrality is imposed, $n_e(y) = n_p(y) = n(y)$. In other words, the electric field is zero at the initial time. Moreover, from (5.3)–(5.4) we have,

$$u_{e,0} = -\frac{u_0}{1 + T_p/T_e}, \tag{5.5}$$

$$u_{p,0} = \frac{u_0}{1 + T_e/T_p}. \tag{5.6}$$

It is worth pointing out that this is not an exact Vlasov kinetic equilibrium. In particular, it differs from the equilibrium presented by Harris since in this simulation the spatial domain is periodic in the varying y-direction. On the other hand, the initial configuration is in force balance and we have checked that the initial equilibrium is not significantly affected by, for example, ballistic effects within the time scale of reconnection considered here. As for the GEM challenge (Birn *et al.* 2001), fluctuations are superposed on the initial magnetic field in order to obtain a single magnetic island at the centre of the space domain at the initial time. In particular, $\delta \boldsymbol{B} = \nabla \delta\psi \times \hat{z}$ and

$$\delta\psi(x, y) = \psi_0 \cos(2\pi x/L_x) \cos(2\pi y/L_y), \tag{5.7}$$

where, as already stated, L_x and L_y are the lengths of the spatial domain in x and y directions, respectively. According to GEM challenge, in scaled units, ψ_0 is set to 0.1.

By using the relation $\delta \boldsymbol{B}(x, y) = \nabla \delta\psi(x, y) \times \hat{z}$ and (2.10), we derive the expression for the current density fluctuations $\delta \boldsymbol{j}(x, y)$ consistent with $\delta\psi(x, y)$. In particular, it is possible to define $\delta \boldsymbol{j}(x, y) = (0, 0, \delta j_z(x, y))$. Finally, the initial electron and proton distribution functions are shifted Maxwellian distributions with drift velocities along the z direction and temperature T_e and T_p.

The phase space has been discretized with $N_x \times N_y = 512 \times 512$ gridpoints in the spatial domain, $N_{e,v_x} \times N_{e,v_y} \times N_{e,v_z} = 41 \times 41 \times 81$ gridpoints in the velocity domain for electrons and $N_{p,v_x} \times N_{p,v_y} \times N_{p,v_z} = 31 \times 31 \times 31$ gridpoints in the velocity domain for protons. We also set $v_e^{\max} = 5 v_{\mathrm{th},e}$ and $v_p^{\max} = 5 v_{\mathrm{th},p}$, where the normalized $v_{\mathrm{th},p}$ is set to 1. Other simulation parameters are $L_1 = 0.5 d_p$, $L_2 = 2.5 d_p$, $m_p/m_e = 25$, $n_\infty = 0.2$, $T_e/T_p = 0.2$, $L_x = L_y = 25.6 d_p$. Also, we set $B_0 = 1$ and $n_0 = 1$. All parameters are chosen to be as close as possible to the simulation parameters listed in Birn *et al.* (2001).

In figure 7 we show the evolution of the reconnected flux given by the difference $\Delta\psi$ between the magnetic flux ψ evaluated at the X point and at the O point. Accordingly to the initial perturbation, the X-point and the O point are initially

https://doi.org/10.1017/S0022377819000631 Published online by Cambridge University Press

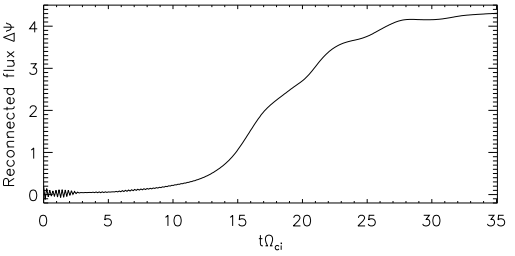


FIGURE 7. Time evolution of the reconnected magnetic flux $\Delta\psi$.

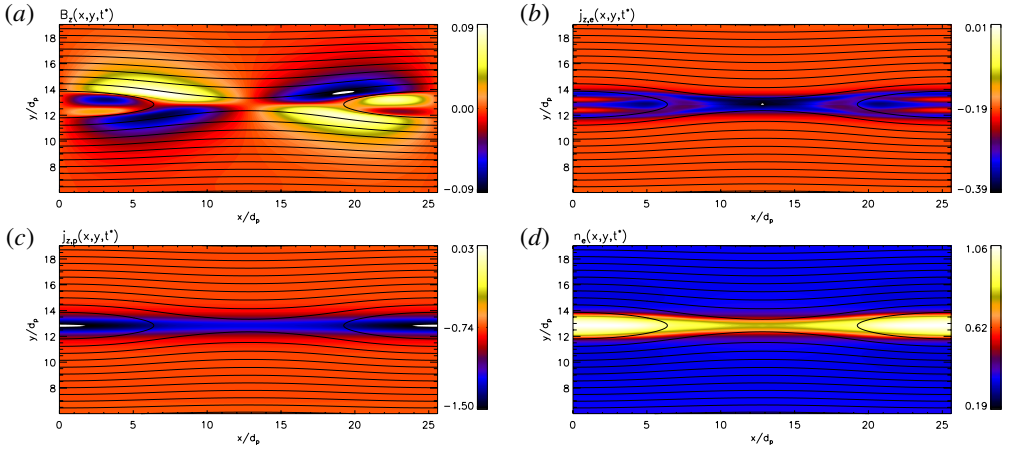


FIGURE 8. Contour plots of B_z (a); out-of-plane electron current density $j_{e,z}$ (b); out-of-plane proton current density $j_{p,z}$ (c); and electron number density n_e (d). The quantities are shown at the time $t^* = 15.27\Omega_{c,p}^{-1}$. At that time $\Delta\psi = 1.18$. All the panels are zoomed in y in the interval $[6d_p, 19d_p]$.

located at $(L_x/2, L_y/2)$ and $(0, L_y/2)$ and their locations do not significantly change throughout the simulation run. The behaviour of $\Delta\psi$ is very similar to the evolution of the reconnected flux in Birn *et al.* (2001). Reconnection evolves with a reconnected flux that remains close to zero until $t \sim 15\Omega_{c,p}^{-1}$, when a sharp increase is observed. Then, the reconnection rate stays relatively constant until the reconnected flux begins to saturate at $t \sim 30\Omega_{c,p}^{-1}$.

In figure 8 we show the contour plots of the out-of-plane magnetic field B_z (a), of the electron current density in the z-direction $j_{e,z}$ (b), of the proton current density in the z-direction $j_{p,z}$ (c) and of the electron number density n_e (d). In each panel, the contour lines of the magnetic flux ψ are superposed; B_z exhibits the typical Hall quadrupolar pattern usually observed during symmetric magnetic reconnection. This magnetic signature indicates that the ions are demagnetized while the electrons are still frozen to the magnetic field. The difference in their dynamics produces the out-of-plane B_z (Mandt, Denton & Drake 1994; Uzdensky & Kulsrud 2006). The quadrupolar structure that we find is analogous to the one obtained with other kinetic codes, both Eulerian (Schmitz & Grauer 2006*b*, see figure 2) and Lagrangian (Pritchett 2001, see Plate 1(*b*)). We note that the $j_{p,z}$ pattern closely follows the density pattern ($n_e \simeq n_p$) so that $j_{p,z}$ is depleted at the X point while it reaches its

https://doi.org/10.1017/S0022377819000631 Published online by Cambridge University Press

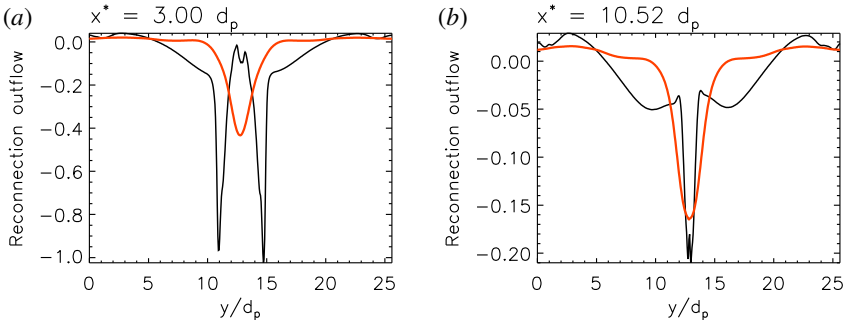


FIGURE 9. (*a*) The x component of the electron velocity u_e (black line) and of the proton velocity u_p (red line) at $x^* = 3.00d_p$ and (*b*) at $x^* = 10.52d_p$. The quantities are shown at the time $t^* = 18.13\Omega_{c,p}^{-1}$.

maximum value within the magnetic island. On the other hand, $j_{e,z}$ is enhanced at the X point and the region of strong $j_{e,z}$ is elongated along x. Away from the X point, $j_{e,z}$ splits into two branches that identify the separatrices, as it was also observed by Shay *et al.* (2001) (see their figure 6*d*). The electron current at the X line has a thickness comparable to d_p which corresponds to $5d_e$. The maximum value of the normalized B_z is 0.09 while the maximum values of $j_{p,z}$ and $j_{e,z}$ are 0.39 and 1.49, respectively. These values are overall slightly smaller than the values found in a similar Vlasov–Darwin simulation described in Schmitz & Grauer (2006*b*).

In figure 9 we show the reconnection outflow of protons and electrons at $t^* = 18.13\Omega_{c,p}$. In particular, we note that at $x = 3d_p$ (panel (*a*)), corresponding to a distance of $9.8d_p$ from the X-point located at $L_x/2 = 12.8d_p$, the electron velocity is characterized by two peaks corresponding to the separatrices, while the proton velocity is concentrated in the centre of the outflow region and it reaches lower values, as expected. The presence of the two peaks is consistent with the $j_{e,z}$ pattern shown in figure 8(*b*). Figure 9(*b*) shows the same quantities of figure 9(*a*) at a distance of $2.3d_p$ from the X-point where the outflow is still developing and we note that $u_{e,x}$ is rather similar in shape and value to $u_{p,x}$.

6. Performance test on the ViDA code

In this section, we present preliminary performance tests of ViDA implemented on the Marconi-KNL cluster at the CINECA supercomputing centre (Casalecchio di Reno (BO), Italy). The Marconi cluster is equipped with 3600 Lenovo Adam Pass nodes, interconnected through the Intel OmniPath network and each one composed of a 1KNL processor (68 cores, 1.40 GHz), formally 96 GB of RAM (effective 83 GB) and 16 GB of MCDRAM. The tests have been performed on a simple equilibrium configuration (Maxwellian DFs with no perturbations). We remark however that this choice does not affect the code performance.

ViDA numerically integrates the VD equations in a six-dimensional phase space (3*D*–3*V*: x, y, z, v_x, v_y, v_z). Only the three-dimensional physical space is parallelized using cubic cells (squared in the two-dimensional configuration). For implementing these tests, we have chosen 51^3 velocity gridpoints for each particle DF (protons and electrons), which represent a typical value adopted in production runs, and we have performed approximately 100 time steps per test (note that changing the step number does not act on the code scalability). Note that two DFs are advanced in time

https://doi.org/10.1017/S0022377819000631 Published online by Cambridge University Press

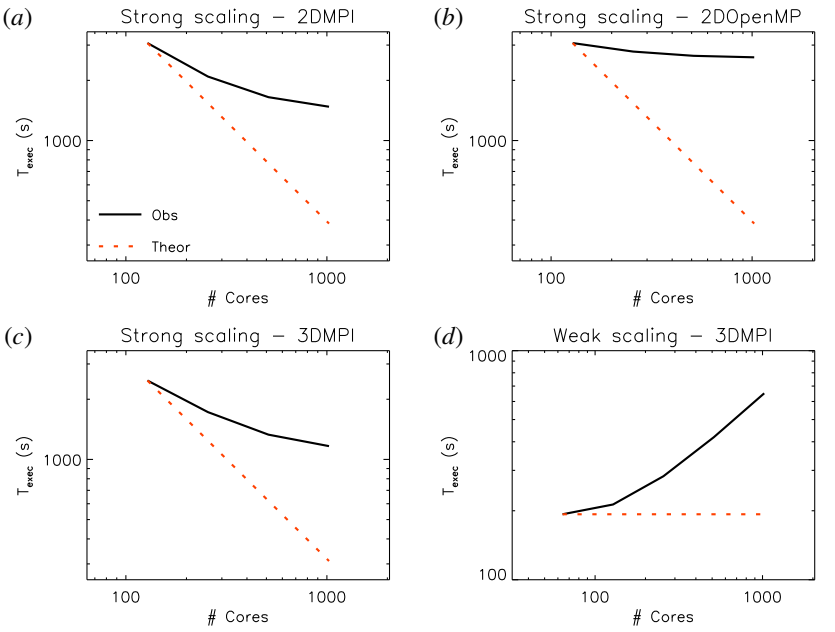


FIGURE 10. (*a*) Strong scaling from 128 to 1024 cores on Marconi KNL using 2 OpenMP threads per Task MPI on the 2.5-dimensional set-up. (*b*) Strong scaling using 64 MPI task and from 2 to 16 OpenMP Threads per task on the 2.5-dimensional set-up. (*c*) Strong scaling from 128 to 1024 cores on Marconi KNL using 2 OpenMP threads per Task MPI on the three-dimensional set-up. (*d*) Weak scaling from 64 to 1024 cores on Marconi KNL using 2 OpenMP threads per Task MPI on the three-dimensional set-up.

through the ViDA algorithm, this limiting the number of spatial grid points per single processor and hence increasing the number of communications.

As a first step, we have analysed the parallel performance in the $2D$–$3V$ configuration, adopting a physical-space grid with 1024×1024 points. This set-up requires approximately 6 TB of RAM, corresponding to, at least, 64 Marconi-KNL nodes. We have performed a strong scaling test by reducing the number of MPI tasks per node from 8 to 1 and maintaining the same number of two OpenMP threads per task. Results are presented in figure 10(*a*): the parallel efficiency scales efficiently up to 512 cores. As the number of cores increases, the efficiency is degraded owing to the more significant weight of MPI communications. This is mainly due to the huge memory request of the code combined with the Marconi KNL architecture. The code performance would strongly benefit from using a computer architecture with a larger RAM and a lower number of cores per node. We have also verified that the performance degradation cannot be handled by using an OpenMP strategy, as shown in figure 10(*b*), since the code performance is not affected by increasing the number of threads per node. In summary, within the current parallelization, the best performance is achieved with 32 MPI threads and 2 OpenMP tasks per node on a KNL system.

A slightly better performance is achieved using a full three-dimensional configuration with $128 \times 128 \times 64$ grid points in the spatial domain. The strong scaling from 128 to 1024 cores is shown in figure 10(*c*). A weak scaling test has been also performed by multiplying the number of spatial points and the number of cores

https://doi.org/10.1017/S0022377819000631 Published online by Cambridge University Press

(nodes) by the same factor. From the results, presented in figure 10(*d*), it can be appreciated that the parallel efficiency is high only up to several hundred cores.

These preliminary tests show a reasonable parallel efficiency on KNL architecture, at least up to some hundreds of cores. We are presently working to increase the code efficiency, in particular optimizing the communication pattern of the ViDA algorithm. We note that these results in part depend on the employed architecture. It is worth finally highlighting that, for instance, by using a Skylake machine with 192 GB and 48 cores per node, we would be able to increase by a factor of 3 the number of spatial gridpoints per node, thus increasing the parallel efficiency of the code, as the number of communications would strongly decrease.

Concerning the computational costs, the ViDA code is approximately twice as computationally expensive as the HVM code (Valentini *et al.* 2007), which has been recently used for three-dimensional simulations of plasma turbulence (see for instance Cerri *et al.* (2018)). More specifically, the reconnection run presented here – which is the most expensive test in this paper in terms of required computational resources – has a cost of slightly less than 0.1 Mh on a Marconi supercomputer using 16 nodes and 512 MPI processes. On the other hand, with ViDA being a code for a new piece of physics, it is difficult to foresee the exact cost of a three-dimensional reconnection (or turbulence) run because the numerical and physical parameters, as well as the duration of the run, can vary significantly with respect to the standard ones used with the HVM code. Based on the experience with the HVM code, we may suggest that a high-resolution three-dimensional run of magnetic reconnection focusing on the electron physics would take from a few to a few tens of Mh. Such a significant allocation of computing time can be obtained, for example, in the framework of a PRACE project.

7. Conclusion

In this paper we have presented a fully kinetic code (ViDA) based on a Vlasov–Darwin algorithm, where only light waves are excluded in order to relax the constraint on the time step advancement. This approach is particularly suited for the investigation of the kinetic dynamics from sub-ion scales down to the electron kinetic scales d_e and to the Debye length λ_D. As typically the case for space plasmas, but often also in the laboratory, inter-particle collisions are not described, since collisional effects are assumed to be insignificant.

ViDA has been tested against several waves modes, in particular Alfvén, whistlers and plasma waves. The development of the Weibel instability and reconnection, both in a regime where the main dynamics is driven by the electrons, has been also reproduced. These tests represent typical regimes of interest for studying the electron-scale kinetic dynamics representing today a strong computational challenge and a frontier problem for the understanding of electron plasma physics.

One of the main future objectives of ViDA will be the study of the structure and dynamics of the electron diffusion region, including the role of anomalous resistivity in Ohm's law and the mechanisms of electron heating, which are among the main targets of satellite MMS data analysis (Torbert *et al.* 2016; Genestreti *et al.* 2018; Cozzani *et al.* 2019). Last but not least, we will make use of the ViDA code for the study of the plasma turbulent dynamics focusing on the problem of the 'dissipative' scale, of primary interest in the context of the solar-wind turbulent heating at kinetic scales (Vaivads *et al.* 2016).

https://doi.org/10.1017/S0022377819000631 Published online by Cambridge University Press

Acknowledgements

This project (F.C., A.R., F.V.) has received funding from the European Unions Horizon 2020 research and innovation programme under grant agreement no. 776262 (AIDA, www.aida-space.eu). O.P. is partly supported by the International Space Science Institute (ISSI) in the framework of the International Team 405 entitled 'Current Sheets, Turbulence, Structures and Particle Acceleration in the Heliosphere'. E.C. is partially supported by NWO Vidi grant 639.072.716. Numerical simulations discussed here have been performed on the Marconi cluster at CINECA (Italy), under the ISCRA initiative (IsC53_MRVDS and IsB16_VDMMS) and under the INAF-CINECA initiative (INA17_C2A16 and INA17_C2A16b).

REFERENCES

BARNES, A. 1966 Collisionless damping of hydromagnetic waves. *Phys. Fluids* **9** (8), 1483–1495.

BIRDSALL, C. K. & LANGDON, A. B. 2004 *Plasma Physics Via Computer Simulation*. CRC press.

BIRN, J., DRAKE, J., SHAY, M., ROGERS, B., DENTON, R., HESSE, M., KUZNETSOVA, M., MA, Z., BHATTACHARJEE, A., OTTO, A. *et al.* 2001 Geospace environmental modeling (GEM) magnetic reconnection challenge. *J. Geophys. Res.* **106** (A3), 3715–3719.

BREUILLARD, H., MATTEINI, L., ARGALL, M. R., SAHRAOUI, F., ANDRIOPOULOU, M., CONTEL, O. L., RETINÒ, A., MIRIONI, L., HUANG, S. Y., GERSHMAN, D. J. *et al.* 2018 New insights into the nature of turbulence in the Earth's magnetosheath using magnetospheric MultiScale mission data. *Astrophys. J.* **859** (2), 127.

BRUNETTI, M., CALIFANO, F. & PEGORARO, F. 2000 Asymptotic evolution of nonlinear Landau damping. *Phys. Rev.* E **62**, 4109–4114.

BRUNO, R. & CARBONE, V. 2016 *Turbulence in the Solar Wind*. Springer.

BURCH, J. L., MOORE, T. E., TORBERT, R. B. & GILES, B. L. 2016*a* Magnetospheric multiscale overview and science objectives. *Space Sci. Rev.* **199**, 5–21.

BURCH, J. L., TORBERT, R. B., PHAN, T. D., CHEN, L.-J., MOORE, T. E., ERGUN, R. E., EASTWOOD, J. P., GERSHMAN, D. J., CASSAK, P. A., ARGALL, M. R. *et al.* 2016*b* Electron-scale measurements of magnetic reconnection in space. *Science* **352** (6290), aaf2939.

CALIFANO, F., CERRI, S., FAGANELLO, M., LAVEDER, D. & KUNZ, M. 2018 Electron-only magnetic reconnection in plasma turbulence, Preprint, arXiv:1810.03957.

CALIFANO, F., FAGANELLO, M. & PEGORARO, F. 2007 Collisionless magnetic reconnection. *Plasma Phys. Control. Fusion* **49** (12B), B439–B446.

CALIFANO, F., HELLINGER, P., KUZNETSOV, E., PASSOT, T., SULEM, P. L. & TRVNEK, P. M. 2008 Nonlinear mirror mode dynamics: simulations and modeling. *J. Geophys. Res.* **113** (A8), A08219.

CALIFANO, F. & MANGENEY, A. 2008 A one dimensional, electrostatic Vlasov model for the generation of suprathermal electron tails in solar wind conditions. *J. Geophys. Res.* **113** (A6), A06103.

CAMPOREALE, E. & BURGESS, D. 2011 The dissipation of solar wind turbulent fluctuations at electron scales. *Astrophys. J.* **730** (2), 114.

CAMPOREALE, E. & BURGESS, D. 2017 Comparison of linear modes in kinetic plasma models. *J. Plasma Phys.* **83** (2), 535830201.

CAMPOREALE, E. & ZIMBARDO, G. 2015 Wave–particle interactions with parallel whistler waves: nonlinear and time-dependent effects revealed by particle-in-cell simulations. *Phys. Plasmas* **22** (9), 092104.

CERRI, S. S. & CALIFANO, F. 2017 Reconnection and small-scale fields in 2D–3V hybrid-kinetic driven turbulence simulations. *New J. Phys.* **19** (2), 025007.

CERRI, S. S., KUNZ, M. W. & CALIFANO, F. 2018 Dual phase-space cascades in 3D hybrid-Vlasov–Maxwell turbulence. *Astrophys. J.* **856** (1), L13.

CERRI, S. S., SERVIDIO, S. & CALIFANO, F. 2017 Kinetic cascade in solar–wind turbulence: 3D3V hybrid-kinetic simulations with electron inertia. *Astrophys. J.* **846** (2), L18.

https://doi.org/10.1017/S0022377819000631 Published online by Cambridge University Press

Chasapis, A., Matthaeus, W. H., Parashar, T. N., Wan, M., Haggerty, C. C., Pollock, C. J., Giles, B. L., Paterson, W. R., Dorelli, J., Gershman, D. J. *et al.* 2018 *In situ* observation of intermittent dissipation at kinetic scales in the Earth's magnetosheath. *Astrophys. J.* **856** (1), L19.

Chen, G. & Chacón, L. 2014 An energy- and charge-conserving, nonlinearly implicit, electromagnetic 1D–3V Vlasov–Darwin particle-in-cell algorithm. *Comput. Phys. Commun.* **185** (10), 2391–2402.

Chen, G. & Chacón, L. 2015 A multi-dimensional, energy- and charge-conserving, nonlinearly implicit, electromagnetic Vlasov–Darwin particle-in-cell algorithm. *Comput. Phys. Commun.* **197**, 73–87.

Cheng, C.-Z. & Knorr, G. 1976 The integration of the Vlasov equation in configuration space. *J. Comput. Phys.* **22** (3), 330–351.

Cozzani, G., Retinò, A., Califano, F., Alexandrova, A., Le Contel, O., Khotyaintsev, Y., Vaivads, A., Fu, H. S., Catapano, F., Breuillard, H. *et al.* 2019 *In situ* spacecraft observations of a structured electron diffusion region during magnetopause reconnection. *Phys. Rev.* E **99**, 043204.

Daughton, W., Roytershteyn, V., Karimabadi, H., Yin, L., Albright, B., Bergen, B. & Bowers, K. 2011 Role of electron physics in the development of turbulent magnetic reconnection in collisionless plasmas. *Nat. Phys.* **7** (7), 539–542.

Delzanno, G. 2015 Multi-dimensional, fully-implicit, spectral method for the Vlasov–Maxwell equations with exact conservation laws in discrete form. *J. Comput. Phys.* **301**, 338–356.

Divin, A., Khotyaintsev, Y. V., Vaivads, A., Andr, M., Markidis, S. & Lapenta, G. 2015 Evolution of the lower hybrid drift instability at reconnection jet front. *J. Geophys. Res.* **120** (4), 2675–2690.

Falchetto, G. L., Scott, B. D., Angelino, P., Bottino, A., Dannert, T., Grandgirard, V., Janhunen, S., Jenko, F., Jolliet, S., Kendl, A. *et al.* 2008 The European turbulence code benchmarking effort: turbulence driven by thermal gradients in magnetically confined plasmas. *Plasma Phys. Control. Fusion* **50** (12), 124015.

Franci, L., Landi, S., Matteini, L., Verdini, A. & Hellinger, P. 2016 Plasma beta dependence of the ion-scale spectral break of solar wind turbulence: high-resolution 2D hybrid simulations. *Astrophys. J.* **833** (1), 91.

Franci, L., Landi, S., Verdini, A., Matteini, L. & Hellinger, P. 2018 Solar wind turbulent cascade from MHD to sub-ion scales: large-size 3D hybrid particle-in-cell simulations. *Astrophys. J.* **853** (1), 26.

Franci, L., Verdini, A., Matteini, L., Landi, S. & Hellinger, P. 2015 Solar wind turbulence from MHD to sub-ion scales: high-resolution hybrid simulations. *Astrophys. J. Lett.* **804**, L39.

Fuselier, S. A., Lewis, W. S., Schiff, C., Ergun, R., Burch, J. L., Petrinec, S. M. & Trattner, K. J. 2016 Magnetospheric multiscale science mission profile and operations. *Space Sci. Rev.* **199** (1), 77–103.

Galeotti, L. & Califano, F. 2005 Asymptotic evolution of weakly collisional Vlasov–Poisson plasmas. *Phys. Rev. Lett.* **95**, 015002.

Galeotti, L., Califano, F. & Pegoraro, F. 2006 Echography of Vlasov codes. *Phys. Lett.* A **355** (4), 381–385.

Gary, S. P. & Karimabadi, H. 2006 Linear theory of electron temperature anisotropy instabilities: whistler, mirror, and Weibel. *J. Geophys. Res. Space Phys.* **111** (A11), A11224.

Genestreti, K. J., Varsani, A., Burch, J. L., Cassak, P. A., Torbert, R. B., Nakamura, R., Ergun, R. E., Phan, T.-D., Toledo-Redondo, S., Hesse, M. *et al.* 2018 Mms observation of asymmetric reconnection supported by 3-D electron pressure divergence. *J. Geophys. Res.* **123** (3), 1806–1821.

Ghizzo, A., Sarrat, M. & Del Sarto, D. 2017 Vlasov models for kinetic Weibel-type instabilities. *J. Plasma Phys.* **83** (1), 705830101.

González, C. A., Parashar, T. N., Gomez, D., Matthaeus, W. H. & Dmitruk, P. 2019 Turbulent electromagnetic fields at sub-proton scales: two-fluid and full-kinetic plasma simulations. *Phys. Plasmas* **26** (1), 012306.

Griffiths, D. J. 1962 *Introduction to Electrodynamics*. Prentice Hall.

https://doi.org/10.1017/S0022377819000631 Published online by Cambridge University Press

GROŠELJ, D., CERRI, S. S., NAVARRO, A. B., WILLMOTT, C., TOLD, D., LOUREIRO, N. F., CALIFANO, F. & JENKO, F. 2017 Fully kinetic versus reduced-kinetic modeling of collisionless plasma turbulence. *Astrophys. J.* **847** (1), 28.

HAGGERTY, C. C., PARASHAR, T. N., MATTHAEUS, W. H., SHAY, M. A., YANG, Y., WAN, M., WU, P. & SERVIDIO, S. 2017 Exploring the statistics of magnetic reconnection *x*-points in kinetic particle-in-cell turbulence. *Phys. Plasmas* **24** (10), 102308.

HARRIS, E. G. 1962 On a plasma sheath separating regions of oppositely directed magnetic field. *Il Nuovo Cimento* **23** (1), 115–121.

HELANDER, P., ERIKSSON, L.-G. & ANDERSSON, F. 2002 Runaway acceleration during magnetic reconnection in tokamaks. *Plasma Phys. Control. Fusion* **44** (12B), B247–B262.

HESSE, M., AUNAI, N., BIRN, J., CASSAK, P., DENTON, R. E., DRAKE, J. F., GOMBOSI, T., HOSHINO, M., MATTHAEUS, W., SIBECK, D. *et al.* 2016 Theory and modeling for the magnetospheric multiscale mission. *Space Sci. Rev.* **199** (1), 577–630.

HOILIJOKI, S., PALMROTH, M., WALSH, B. M., PFAU-KEMPF, Y., VONÂ ALFTHAN, S., GANSE, U., HANNUKSELA, O. & VAINIO, R. 2016 Mirror modes in the Earth's magnetosheath: results from a global hybrid-Vlasov simulation. *J. Geophys. Res. Space Phys.* **121** (5), 4191–4204.

HOWES, G., DORLAND, W., COWLEY, S., HAMMETT, G., QUATAERT, E., SCHEKOCHIHIN, A. & TATSUNO, T. 2008*a* Kinetic simulations of magnetized turbulence in astrophysical plasmas. *Phys. Rev. Lett.* **100** (6), 065004.

HOWES, G. G. 2016 The dynamical generation of current sheets in astrophysical plasma turbulence. *Astrophys. J. Lett.* **827** (2), L28.

HOWES, G. G., COWLEY, S. C., DORLAND, W., HAMMETT, G. W., QUATAERT, E. & SCHEKOCHIHIN, A. A. 2008*b* A model of turbulence in magnetized plasmas: implications for the dissipation range in the solar wind. *J. Geophys. Res.* **113** (A5), A05103.

HOWES, G. G., COWLEY, S. C., DORLAND, W., HAMMETT, G. W., QUATAERT, E. & SCHEKOCHIHIN, A. E A. 2006 Astrophysical gyrokinetics: basic equations and linear theory. *Astrophys. J.* **651** (1), 590–614.

HOWES, G. G., TENBARGE, J. M., DORLAND, W., QUATAERT, E., SCHEKOCHIHIN, A. A., NUMATA, R. & TATSUNO, T. 2011 Gyrokinetic simulations of solar wind turbulence from ion to electron scales. *Phys. Rev. Lett.* **107** (3), 035004.

JUNO, J., HAKIM, A., TENBARGE, J., SHI, E. & DORLAND, W. 2018 Discontinuous galerkin algorithms for fully kinetic plasmas. *J. Comput. Phys.* **353**, 110–147.

KARIMABADI, H., ROYTERSHTEYN, V., WAN, M., MATTHAEUS, W. H., DAUGHTON, W., WU, P., SHAY, M., LORING, B., BOROVSKY, J. & LEONARDIS, E. 2013 Coherent structures, intermittent turbulence, and dissipation in high-temperature plasmas. *Phys. Plasmas* **20** (1), 012303.

KAUFMAN, A. N. & ROSTLER, P. S. 1971 The Darwin model as a tool for electromagnetic plasma simulation. *Phys. Fluids* **14** (2), 446–448.

KEMPF, Y., POKHOTELOV, D., VON ALFTHAN, S., VAIVADS, A., PALMROTH, M. & KOSKINEN, H. E. J. 2013 Wave dispersion in the hybrid-Vlasov model: verification of Vlasiator. *Phys. Plasmas* **20** (11), 112114.

KOBAYASHI, S., SAHRAOUI, F., PASSOT, T., LAVEDER, D., SULEM, P. L., HUANG, S. Y., HENRI, P. & SMETS, R. 2017 Three-dimensional simulations and spacecraft observations of sub-ion scale turbulence in the solar wind: influence of Landau damping. *Astrophys. J.* **839** (2), 122.

KRALL, N. A. & TRIVELPIECE, A. W. 1973 Principles of plasma physics. *Am. J. Phys.* **41** (12), 1380–1381.

KULSRUD, R. M. 2005 *Plasma Physics for Astrophysics*. Princeton University Press.

LANDAU, L. 1946 On the vibration of the electronic plasma. *Zh. Eksp. Teor. Fiz.* **16**, 574.

LAPENTA, G., MARKIDIS, S., GOLDMAN, M. V. & NEWMAN, D. L. 2015 Secondary reconnection sites in reconnection-generated flux ropes and reconnection fronts. *Nat. Phys.* **11** (8), 690–695.

LAPENTA, G., PUCCI, F., GOLDMAN, M. V. & NEWMAN, D. L. 2019 A violin sonata for reconnection, Preprint, arXiv:1904.02094.

LE CONTEL, O., RETINÒ, A., BREUILLARD, H., MIRIONI, L., ROBERT, P., CHASAPIS, A., LAVRAUD, B., CHUST, T., REZEAU, L., WILDER, F. D. *et al.* 2016 Whistler mode waves and Hall fields detected by mms during a dayside magnetopause crossing. *Geophys. Res. Lett.* **43** (12), 5943–5952.

https://doi.org/10.1017/S0022377819000631 Published online by Cambridge University Press

LEONARDIS, E., CHAPMAN, S. C., DAUGHTON, W., ROYTERSHTEYN, V. & KARIMABADI, H. 2013 Identification of intermittent multifractal turbulence in fully kinetic simulations of magnetic reconnection. *Phys. Rev. Lett.* **110** (20), 205002.

LYUTIKOV, M. 2003 Explosive reconnection in magnetars. *Mon. Not. R. Astron. Soc.* **346** (2), 540–554.

MANDT, M. E., DENTON, R. E. & DRAKE, J. F. 1994 Transition to whistler mediated magnetic reconnection. *Geophys. Res. Lett.* **21** (1), 73–76.

MANGENEY, A., CALIFANO, F., CAVAZZONI, C. & TRAVNICEK, P. 2002 A numerical scheme for the integration of the Vlasov–Maxwell system of equations. *J. Comput. Phys.* **179** (2), 495–538.

MARKIDIS, S., LAPENTA, G. & RIZWAN-UDDIN 2010 Multi-scale simulations of plasma with ipic3d. *Maths Comput. Simul.* **80** (7), 1509–1519; Multiscale modeling of moving interfaces in materials.

MARSCH, E. 2006 Kinetic physics of the solar corona and solar wind. *Living Rev. Solar Phys.* **3** (1), 1.

NAVARRO, A. B. N, TEACA, B., TOLD, D., GROSELJ, D., CRANDALL, P. & JENKO, F. 2016 Structure of plasma heating in gyrokinetic Alfvénic turbulence. *Phys. Rev. Lett.* **117**, 245101.

O'NEIL, T. 1965 Collisionless damping of nonlinear plasma oscillations. *Phys. Fluids* **8** (12), 2255–2262.

PALMROTH, M., GANSE, U., PFAU-KEMPF, Y., BATTARBEE, M., TURC, L., BRITO, T., GRAND IN, M., HOILIJOKI, S., SANDROOS, A. & VON ALFTHAN, S. 2018 Vlasov methods in space physics and astrophysics. *Living Rev. Comput. Astrophys.* **4** (1), 1.

PALMROTH, M., HONKONEN, I., SANDROOS, A., KEMPF, Y., VON ALFTHAN, S. & POKHOTELOV, D. 2013 Preliminary testing of global hybrid-Vlasov simulation: magnetosheath and cusps under northward interplanetary magnetic field. *J. Atmos. Sol. Terr. Phys.* **99**, 41–46.

PALODHI, L., CALIFANO, F. & PEGORARO, F. 2009 Nonlinear kinetic development of the Weibel instability and the generation of electrostatic coherent structures. *Plasma Phys. Control. Fusion* **51** (12), 125006.

PALODHI, L., CALIFANO, F. & PEGORARO, F. 2010 On the transition between the Weibel and the whistler instabilities. *Plasma Phys. Control. Fusion* **52** (9), 095007.

PARASHAR, T. N., MATTHAEUS, W. H. & SHAY, M. A. 2018 Dependence of kinetic plasma turbulence on plasma β. *Astrophys. J.* **864** (1), L21.

PARASHAR, T. N., SHAY, M. A., CASSAK, P. A. & MATTHAEUS, W. H. 2009 Kinetic dissipation and anisotropic heating in a turbulent collisionless plasma. *Phys. Plasmas* **16** (3), 032310.

PASSOT, T. & SULEM, P. L. 2007 Collisionless magnetohydrodynamics with gyrokinetic effects. *Phys. Plasmas* **14** (8), 082502.

PERRONE, D., PASSOT, T., LAVEDER, D., VALENTINI, F., SULEM, P. L., ZOUGANELIS, I., VELTRI, P. & SERVIDIO, S. 2018 Fluid simulations of plasma turbulence at ion scales: comparison with Vlasov–Maxwell simulations. *Phys. Plasmas* **25** (5), 052302.

PEYRET, R. & TAYLOR, T. D. 1986 *Computational Methods for Fluid Flow*, Springer Series in Computational Physics. Springer.

PEZZI, O., PARASHAR, T. N., SERVIDIO, S., VALENTINI, F., VÁSCONEZ, C. L., YANG, Y., MALARA, F., MATTHAEUS, W. H. & VELTRI, P. 2017*a* Colliding Alfvénic wave packets in magnetohydrodynamics, Hall and kineticsimulations. *J. Plasma Phys.* **83** (1), 705830108.

PEZZI, O., PARASHAR, T. N., SERVIDIO, S., VALENTINI, F., VÁSCONEZ, C. L., YANG, Y., MALARA, F., MATTHAEUS, W. H. & VELTRI, P. 2017*b* Revisiting a classic: the parkermoffatt problem. *Astrophys. J.* **834** (2), 166.

PEZZI, O., PERRONE, D., SERVIDIO, S., VALENTINI, F., SORRISO-VALVO, L. & VELTRI, P. 2019 Proton–proton collisions in the turbulent solar wind: hybrid Boltzmann–Maxwell simulations, Preprint, arXiv:1903.03398.

PEZZI, O., SERVIDIO, S., PERRONE, D., VALENTINI, F., SORRISO-VALVO, L., GRECO, A., MATTHAEUS, W. H. & VELTRI, P. 2018 Velocity-space cascade in magnetized plasmas: numerical simulations. *Phys. Plasmas* **25** (6), 060704.

PEZZI, O., VALENTINI, F. & VELTRI, P. 2016 Collisional relaxation of fine velocity structures in plasmas. *Phys. Rev. Lett.* **116** (14), 145001.

https://doi.org/10.1017/S0022377819000631 Published online by Cambridge University Press

PFAU-KEMPF, Y., BATTARBEE, M., GANSE, U., HOILIJOKI, S., TURC, L., VON ALFTHAN, S., VAINIO, R. & PALMROTH, M. 2018 On the importance of spatial and velocity resolution in the hybrid-Vlasov modeling of collisionless shocks. *Front. Phys.* **6**, 44.

PHAN, T., EASTWOOD, J. P., SHAY, M., DRAKE, J., SONNERUP, B. Ö, FUJIMOTO, M., CASSAK, P., ØIEROSET, M., BURCH, J., TORBERT, R. *et al.* 2018 Electron magnetic reconnection without ion coupling in Earths turbulent magnetosheath. *Nature* **557** (7704), 202.

POKHOTELOV, D., VON ALFTHAN, S., KEMPF, Y., VAINIO, R., KOSKINEN, H. E. J. & PALMROTH, M. 2013 Ion distributions upstream and downstream of the Earth's bow shock: first results from Vlasiator. *Ann. Geophys.* **31** (12), 2207–2212.

PRITCHETT, P. 2008 Collisionless magnetic reconnection in an asymmetric current sheet. *J. Geophys. Res.* **113** (A6), A06210.

PRITCHETT, P. L. 2001 Geospace environment modeling magnetic reconnection challenge: simulations with a full particle electromagnetic code. *J. Geophys. Res.* **106**, 3783–3798.

PUCCI, F., MATTHAEUS, W. H., CHASAPIS, A., SERVIDIO, S., SORRISO-VALVO, L., OLSHEVSKY, V., NEWMAN, D. L., GOLDMAN, M. V. & LAPENTA, G. 2018 Generation of turbulence in colliding reconnection jets. *Astrophys. J.* **867** (1), 10.

PUCCI, F., SERVIDIO, S., SORRISO-VALVO, L., OLSHEVSKY, V., MATTHAEUS, W. H., MALARA, F., GOLDMAN, M. V., NEWMAN, D. L. & LAPENTA, G. 2017 Properties of turbulence in the reconnection exhaust: numerical simulations compared with observations. *Astrophys. J.* **841** (1), 60.

RETINÒ, A., SUNDKVIST, D., VAIVADS, A., MOZER, F., ANDRÉ, M. & OWEN, C. J. 2007 *In situ* evidence of magnetic reconnection in turbulent plasma. *Nat. Phys.* **3**, 236–238.

RINCON, F., CALIFANO, F., SCHEKOCHIHIN, A. A. & VALENTINI, F. 2016 Turbulent dynamo in a collisionless plasma. *Proc. Natl Acad. Sci. USA* **113** (15), 3950–3953.

ROYTERSHTEYN, V., BOLDYREV, S., DELZANNO, G. L., CHEN, C. H. K., GROŠELJ, D. & LOUREIRO, N. F. 2019 Numerical study of inertial kinetic-Alfvén turbulence. *Astrophys. J.* **870** (2), 103.

SCHEKOCHIHIN, A. A., COWLEY, S. C., DORLAND, W., HAMMETT, G. W., HOWES, G. G., PLUNK, G. G., QUATAERT, E. & TATSUNO, T. 2008 Gyrokinetic turbulence: a nonlinear route to dissipation through phase space. *Plasma Phys. Control. Fusion* **50** (12), 124024.

SCHMITZ, H. & GRAUER, R. 2006*a* Darwin–Vlasov simulations of magnetised plasmas. *J. Comput. Phys.* **214** (2), 738–756.

SCHMITZ, H. & GRAUER, R. 2006*b* Kinetic Vlasov simulations of collisionless magnetic reconnection. *Phys. Plasmas* **13** (9), 092309.

SERVIDIO, S., CHASAPIS, A., MATTHAEUS, W. H., PERRONE, D., VALENTINI, F., PARASHAR, T. N., VELTRI, P., GERSHMAN, D., RUSSELL, C. T., GILES, B. *et al.* 2017 Magnetospheric multiscale observation of plasma velocity-space cascade: Hermite representation and theory. *Phys. Rev. Lett.* **119**, 205101.

SERVIDIO, S., MATTHAEUS, W. H., SHAY, M. A., CASSAK, P. A. & DMITRUK, P. 2009 Magnetic reconnection in two-dimensional magnetohydrodynamic turbulence. *Phys. Rev. Lett.* **102** (11), 115003.

SERVIDIO, S., MATTHAEUS, W. H., SHAY, M. A., DMITRUK, P., CASSAK, P. A. & WAN, M. 2010 Statistics of magnetic reconnection in two-dimensional magnetohydrodynamic turbulence. *Phys. Plasmas* **17** (3), 032315.

SERVIDIO, S., VALENTINI, F., CALIFANO, F. & VELTRI, P. 2012 Local kinetic effects in two-dimensional plasma turbulence. *Phys. Rev. Lett.* **108** (4), 045001.

SERVIDIO, S., VALENTINI, F., PERRONE, D., GRECO, A., CALIFANO, F., MATTHAEUS, W. H. & VELTRI, P. 2015 A kinetic model of plasma turbulence. *J. Plasma Phys.* **81** (1), 325810107.

SHAY, M. A., DRAKE, J. F., ROGERS, B. N. & DENTON, R. E. 2001 Alfvénic collisionless magnetic reconnection and the Hall term. *J. Geophys. Res.* **106** (A3), 3759–3772.

SHAY, M. A., HAGGERTY, C. C., MATTHAEUS, W. H., PARASHAR, T. N., WAN, M. & WU, P. 2018 Turbulent heating due to magnetic reconnection. *Phys. Plasmas* **25** (1), 012304.

SKOUTNEV, V., HAKIM, A., JUNO, J. & TENBARGE, J. M. 2019 Temperature-dependent saturation of Weibel-type instabilities in counter-streaming plasmas. *Astrophys. J. Lett.* **872** (2), L28.

https://doi.org/10.1017/S0022377819000631 Published online by Cambridge University Press

SORRISO-VALVO, L., CARBONE, F., PERRI, S., GRECO, A., MARINO, R. & BRUNO, R. 2018*a* On the statistical properties of turbulent energy transfer rate in the inner heliosphere. *Solar Phys.* **293** (1), 10.

SORRISO-VALVO, L., CATAPANO, F., RETINÒ, A., LE CONTEL, O., PERRONE, D., ROBERTS, O. W., COBURN, J. T., PANEBIANCO, V., VALENTINI, F., PERRI, S. *et al.* 2019 Turbulence-driven ion beams in the magnetospheric Kelvin–Helmholtz instability. *Phys. Rev. Lett.* **122**, 035102.

SORRISO-VALVO, L., PERRONE, D., PEZZI, O., VALENTINI, F., SERVIDIO, S., ZOUGANELIS, I. & VELTRI, P. 2018*b* Local energy transfer rate and kinetic processes: the fate of turbulent energy in two-dimensional hybrid Vlasov–Maxwell numerical simulations. *J. Plasma Phys.* **84** (2), 725840201.

SULEM, P. L. & PASSOT, T. 2015 Landau fluid closures with nonlinear large-scale finite Larmor radius corrections for collisionless plasmas. *J. Plasma Phys.* **81** (1), 325810103.

SULEM, P. L., PASSOT, T., LAVEDER, D. & BORGOGNO, D. 2016 Influence of the nonlinearity parameter on the solar wind sub-ion magnetic energy spectrum: FLR-Landau fluid simulations. *Astrophys. J.* **818** (1), 66.

TANABE, H., YAMADA, T., WATANABE, T., GI, K., KADOWAKI, K., INOMOTO, M., IMAZAWA, R., GRYAZNEVICH, M., MICHAEL, C., CROWLEY, B. *et al.* 2015 Electron and ion heating characteristics during magnetic reconnection in the mast spherical tokamak. *Phys. Rev. Lett.* **115**, 215004.

TATSUNO, T., DORLAND, W., SCHEKOCHIHIN, A. A., PLUNK, G. G., BARNES, M., COWLEY, S. C. & HOWES, G. G. 2009 Nonlinear phase mixing and phase-space cascade of entropy in gyrokinetic plasma turbulence. *Phys. Rev. Lett.* **103** (1), 015003.

TENBARGE, J. M., HOWES, G. G. & DORLAND, W. 2013 Collisionless damping at electron scales in solar wind turbulence. *Astrophys. J.* **774** (2), 139.

TOLD, D., JENKO, F., TENBARGE, J. M., HOWES, G. G. & HAMMETT, G. W. 2015 Multiscale nature of the dissipation range in gyrokinetic simulations of Alfvénic turbulence. *Phys. Rev. Lett.* **115** (2), 025003.

TORBERT, R. B., BURCH, J. L., GILES, B. L., GERSHMAN, D., POLLOCK, C. J., DORELLI, J., AVANOV, L., ARGALL, M. R., SHUSTER, J., STRANGEWAY, R. J. *et al.* 2016 Estimates of terms in Ohm's law during an encounter with an electron diffusion region. *Geophys. Res. Lett.* **43** (12), 5918–5925.

TORBERT, R. B., BURCH, J. L., PHAN, T. D., HESSE, M., ARGALL, M. R., SHUSTER, J., ERGUN, R. E., ALM, L., NAKAMURA, R., GENESTRETI, K. J. *et al.* 2018 Electron-scale dynamics of the diffusion region during symmetric magnetic reconnection in space. *Science* **362** (6421), 1391–1395.

TRONCI, C. & CAMPOREALE, E. 2015 Neutral Vlasov kinetic theory of magnetized plasmas. *Phys. Plasmas* **22** (2), 020704.

UMEDA, T., MIWA, J.-I, MATSUMOTO, Y., NAKAMURA, T. K. M., TOGANO, K., FUKAZAWA, K. & SHINOHARA, I. 2010 Full electromagnetic Vlasov code simulation of the Kelvin–Helmholtz instability. *Phys. Plasmas* **17** (5), 052311.

UMEDA, T., TOGANO, K. & OGINO, T. 2009 Two-dimensional full-electromagnetic Vlasov code with conservative scheme and its application to magnetic reconnection. *Comput. Phys. Commun.* **180** (3), 365–374.

UMEDA, T. & WADA, Y. 2016 Secondary instabilities in the collisionless Rayleigh–Taylor instability: full kinetic simulation. *Phys. Plasmas* **23** (11), 112117.

UMEDA, T. & WADA, Y. 2017 Non-MHD effects in the nonlinear development of the MHD-scale Rayleigh–Taylor instability. *Phys. Plasmas* **24** (7), 072307.

UZDENSKY, D. A. 2011 Magnetic reconnection in extreme astrophysical environments. *Space Sci. Rev.* **160** (1), 45–71.

UZDENSKY, D. A. & KULSRUD, R. M. 2006 Physical origin of the quadrupole out-of-plane magnetic field in Hall-magnetohydrodynamic reconnection. *Phys. Plasmas* **13** (6), 062305.

VAIVADS, A., RETINÒ, A., SOUCEK, J., KHOTYAINTSEV, Y. V., VALENTINI, F., ESCOUBET, C. P., ALEXANDROVA, O., ANDRÉ, M., BALE, S. D., BALIKHIN, M. *et al.* 2016 Turbulence heating observer satellite mission proposal. *J. Plasma Phys.* **82** (5), 905820501.

https://doi.org/10.1017/S0022377819000631 Published online by Cambridge University Press

VALENTINI, F., CALIFANO, F. & VELTRI, P. 2010 Two-dimensional kinetic turbulence in the solar wind. *Phys. Rev. Lett.* **104**, 205002.

VALENTINI, F., CARBONE, V., VELTRI, P. & MANGENEY, A. 2005 Self-consistent Lagrangian study of nonlinear Landau damping. *Phys. Rev.* E **71** (1), 017402.

VALENTINI, F., PERRONE, D., STABILE, S., PEZZI, O., SERVIDIO, S., MARCO, R. D., MARCUCCI, F., BRUNO, R., LAVRAUD, B., KEYSER, J. D. *et al.* 2016 Differential kinetic dynamics and heating of ions in the turbulent solar wind. *New J. Phys.* **18** (12), 125001.

VALENTINI, F., TRÁVNÍČEK, P., CALIFANO, F., HELLINGER, P. & MANGENEY, A. 2007 A hybrid-Vlasov model based on the current advance method for the simulation of collisionless magnetized plasma. *J. Comput. Phys.* **225** (1), 753–770.

VALENTINI, F., VÁSCONEZ, C. L., PEZZI, O., SERVIDIO, S., MALARA, F. & PUCCI, F. 2017 Transition to kinetic turbulence at proton scales driven by large-amplitude kinetic Alfvén fluctuations. *Astron. Astrophys.* **599**, A8.

VÀSCONEZ, C. L., VALENTINI, F., CAMPOREALE, E. & VELTRI, P. 2014 Vlasov simulations of kinetic Alfvén waves at proton kinetic scales. *Phys. Plasmas* **21** (11), 112107.

VON ALFTHAN, S., POKHOTELOV, D., KEMPF, Y., HOILIJOKI, S., HONKONEN, I., SANDROOS, A. & PALMROTH, M. 2014 Vlasiator: first global hybrid-Vlasov simulations of Earth's foreshock and magnetosheath. *J. Atmos. Sol.-Terr. Phys.* **120**, 24–35.

WAN, M., MATTHAEUS, W. H., ROYTERSHTEYN, V., KARIMABADI, H., PARASHAR, T., WU, P. & SHAY, M. 2015 Intermittent dissipation and heating in 3D kinetic plasma turbulence. *Phys. Rev. Lett.* **114** (17), 175002.

WEIBEL, E. S. 1959 Spontaneously growing transverse waves in a plasma due to an anisotropic velocity distribution. *Phys. Rev. Lett.* **2**, 83–84.

YANG, Y., MATTHAEUS, W. H., PARASHAR, T. N., HAGGERTY, C. C., ROYTERSHTEYN, V., DAUGHTON, W., WAN, M., SHI, Y. & CHEN, S. 2017 Energy transfer, pressure tensor, and heating of kinetic plasma. *Phys. Plasmas* **24** (7), 072306.

ZEILER, A., BISKAMP, D., DRAKE, J. F., ROGERS, B. N., SHAY, M. A. & SCHOLER, M. 2002 Three-dimensional particle simulations of collisionless magnetic reconnection. *J. Geophys. Res.* **107** (A9), SMP 6-1–SMP 6-9.

https://doi.org/10.1017/S0022377819000631 Published online by Cambridge University Press